Chapter 8

Wettability of Nanostructured Surfaces

L. Duta, A.C. Popescu, I. Zgura, N. Preda and I.N. Mihailescu

Additional information is available at the end of the chapter

http://dx.doi.org/10.5772/60808

Abstract

There are many studies in literature concerning contact angle measurements on different materials/substrates. It is documented that textiles can be coated with multifunctional materials in form of thin films or nanoparticles to acquire characteristics that can improve the protection and comfort of the wearer. The capacity of oxide nanostructures to inhibit fungal development and neutralize bacteria is a direct consequence of their wetting behavior [1–6]. Moreover, the radical modification of wetting behavior of nanostructures from hydrophilic to hydrophobic when changing the pulsed laser deposition (PLD) ambient will be thoroughly discussed.

When an implant is introduced inside the human body, its surface is first wetted by the physiological fluids. This further controls the proteins adsorption followed by the attachment of cells to the implant surface. Hence, surface wettability is considered an important criterion that dictates biocompatibility of the implant and could stand for a decisive factor for its long-term stability inside the human body.

In Section 1 of this chapter, the reader is briefly introduced to wetting phenomenon, and correlations between well-known Young, Cassie, and Wenzel approaches are made. Next, one of the most spread techniques to measure the wettability of surface, the contact angle measurement, is thoroughly explained and relevant examples are given.

Section 2 begins with a summarized table about previous works on synthesis of hydrophobic or hydrophilic nanostructures with a special focus on ZnO, SiO_x, TiO_2, and DLC materials. A short presentation of the advantages of their synthesis by PLD, sol-gel, thermal evaporation, solution based on chemical approaches, sputtering, and plasma enhanced chemical vapor deposition will be introduced.

Sections 3 includes a brief literature overview on results regarding synthesis by aforementioned techniques of different oxides (ZnO, TiO_2, and SiO_x) and DLC nanostructures onto textile (polyester, polyamide, cotton/polyester, and poly(lactic acid)) or metallic substrates for medical purposes.

The chapter ends with conclusions and references, which include books and review articles relevant to the topics.

Keywords: Wettability, contact angle measurements, oxide and diamond like carbon nanostructures, textile functionalization, medical applications, pulsed laser deposition, sol-gel, combined radio frequency plasma enhanced chemical vapor deposition, magnetron sputtering

1. Introduction

Wetting is the ability of liquids to keep in contact with solid surfaces. It is a direct result of intermolecular interactions, which occur when two media (liquid and solid) are brought together. Wettability studies usually involve the measurements of contact angle (CA), which indicates the degree of wetting when a solid and liquid interact. A low CA (<90°) corresponds to high wettability, and the fluid will spread over a large area of the surface. A high CA (>90°) corresponds to low wettability, and the fluid will minimize contact with the surface and form a compact liquid droplet. CA>150° indicates minimal contact between the liquid droplet and the surface and corresponds to a superhydrophobic behavior.

In the case of a liquid droplet on an ideal solid surface (which is flat, rigid, perfectly smooth, chemically homogeneous, and has zero CA hysteresis), which forms a CA (θ), the general formula of the well-known Young's equation (which assumes a perfectly flat and rigid surface) [7] that describes the balance (Figure 1a) between the surface tension of the liquid/vapor γ_{SV} and that of the liquid/vapor γ_{LV} and the interfacial tension of the solid/liquid γ_{LS} is as follows:

$$\cos\theta = \left(\gamma_{SV} - \gamma_{LS}\right) / \gamma_{LV} \tag{1}$$

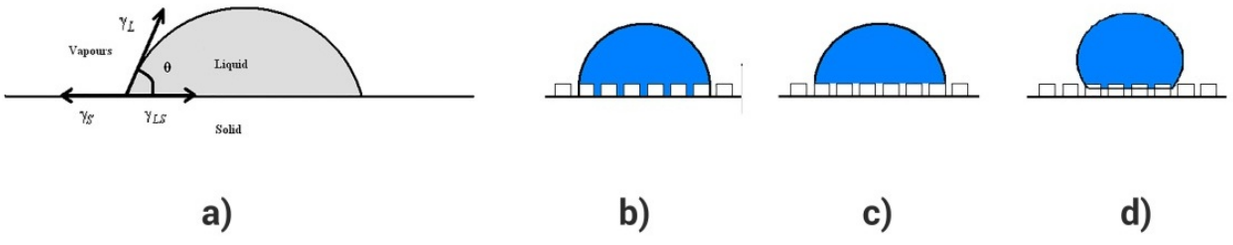

Figure 1. Wetting behavior of solid substrates: (a) Young, (b) Wenzel, (c) Cassie, and (d) intermediate state between Wenzel and Cassie regimes.

In reality, only a few solid surfaces are actually flat. The surface roughness is therefore one important parameter that should be taken into consideration when assessing the wetting behavior of a surface [8, 9]. This influence can prove significant for static and dynamic wetting.

Besides Young's theory, the Wenzel (Figure 1b) and Cassie (Figure 1c) regimes [9, 10], or an intermediate state between these two models (Figure 1d) [11], are generally used to correlate the roughness of the surface with the apparent CA of a liquid.

Several authors modeled the effect of surface roughness over CA [12–14]. The basic idea was to account for roughness through r, which is the ratio of the actual to projected area. Thus, $A_{LS}=r \cdot A_{LSapp}$ and $A_{SV}=r \cdot A_{SVapp}$ where A_{LS} and A_{SV} are the liquid-solid and solid-vapor areas, A_{LSapp} and A_{SVapp} are the liquid-solid and solid-vapor areas. In this case, Eq. (1) becomes

$$\cos\theta_{rough} = r\cos\theta_{true} \tag{2}$$

Due to surface roughness, for CA <90°, the apparent CA will decrease, while for CA>90°, its value will increase. This corresponds to the Wenzel case, as illustrated in Figure 1b, where the liquid completely fills the air pockets of the rough surface at the contact site. If the CA is large and the surface rough, the liquid may trap air. As a consequence, a composite surface effect will appear, as illustrated in Figure 1c.

In the Cassie model [15], it is presumed that in the grooves the air is trapped under the liquid droplet. This determines the appearance of a composite surface (Figure 1c). The chemical heterogeneity of a rough surface can be related, in this model, to the apparent CA, θ_{app}, through the following formula:

$$\cos\theta_{app} = f_S\cos\theta_S + f_V\cos\theta_V \tag{3}$$

with f_S and f_V as the area fractions of the solid and vapor on the surface, respectively. Since $f_S + f_V = 1$, $\theta_S = \theta$, and $\theta_V = 180°$, Eq. (3) can be written as follows:

$$\cos\theta_{app} = -1 + f_S\left(\cos\theta_{true} + 1\right) \tag{4}$$

where θ_{true} is the CA on a smooth surface [15].

From Eq. (4), it follows that in case of a true value of CA >90°, the surface roughness will determine an increase of CA's apparent value. In contradiction to Wenzel regime, in the Cassie mode, the CA value will increase even for CA values <90º due to the air pockets trapped under the liquid droplet [9]. It was shown that, when applying a physical deformation to a spherical droplet, a variation from the Cassie to Wenzel state can be achieved [16, 17] (Figure 1d). In some cases, a transition between these two modes can also occur [18–20]. Therefore, the droplet will fill the air pockets of the rough substrate resulting in a decrease of the apparent value of CA. In these cases, for the estimation of CA values, Eqs. (2) and (4) can be used before and after the transition, respectively. Taking into account these results, the following equation can be written [11]:

$$\cos\theta_{th} = \left(f_S - 1\right) / \left(r - f_S\right) \tag{5}$$

where θ_{th} represents a threshold value between Wenzel and Cassie states.

1.1. CA measurements of nanostructured surfaces

Immediately after an implant is introduced inside the human body, the first events that occur are the wetting of the material by the physiological fluids, followed by attachment of cells to the implant surface [21]. In order to evaluate the wetting behavior of a system, plenty of quantitative (CA, imbibition, and forced displacement, and electrical resistivity wettability) and qualitative (imbibition rates, microscope examination, flotation, glass slide, relative permeability curves, permeability/saturation relationships, capillary pressure curves, capillarimetric method, displacement capillary pressure, reservoir logs, nuclear magnetic resonance, and dye adsorption) methods have been developed [22]. Among these, CA measurement is probably the most adopted technique to investigate the average wettability of a surface [23]. Moreover, this type of investigation has been extensively applied to assess the wetting behavior of different nanostructured surfaces, used for various medical applications. Some relevant literature examples limited to oxides (ZnO, TiO_2, SiO_x) and diamond-like carbon (DLC) structures are briefly summarized in Table 1.

Material	Envisaged application	Cited reference
ZnO	Self-cleaning coatings and antifogging materials	[24]
	Antibacterial properties	[25, 26]
	Environmental sensing	[27]
	Micro/nanodevices	[28]
SiO_x	Antibacterial properties	[29]
	Cells migration on artificial surfaces	[30]
	Bioactive properties	[31]
	Superoleophobic surfaces	[32]
TiO_2	Antibacterial properties	[25]
	Microbial fuel cells and bioremediations	[33]
	Blood-contacting biomaterials	[34]
DLC	Temporary blood-contacting medical devices (cardiovascular and interventional devices, artificial organs, pacemakers)	[35, 36]
	Femoral head and the acetabulum hip joint components	[37]
	Resistance to corrosion	[38]
	Antifogging	[39]
	Resistance to microbial adhesion	[40]

Table 1. CA measurements of hydrophobic/hydrophilic ZnO, SiO_x, TiO_2, and DLC nanostructures used for medical applications.

CA can be classified into static or dynamic. Static CA is measured when liquid droplet is standing alone on the surface, without needle insertion, and the solid/liquid/air boundary is not moving. These measurements are used in quality control and research and product development. One can measure the dynamic CA when the solid/liquid/air boundary is moving. In this way, advancing and receding CA are measured. CA hysteresis, which represents the difference between these two angles, comes from surface chemical and topographical heterogeneities, solution impurities absorbing on the surface, or swelling, rearrangement or alteration of the surface by the solvent [41, 42].

The hydrophobic behavior of a surface is generally assessed by the apparent water CA, in static measurements. Moreover, when evaluating a surface repellency, one should take into consideration the sliding-down (which is evaluated by measuring the sliding angle, α, at which a liquid droplet begins to slide down an inclined plate) and rolling-off behaviors of liquid droplets [9]. Due to the CA hysteresis [43, 44], the liquid droplets do not slide off easily on a surface presenting a high value of static CA. Eq. (6) [43, 45] quantitatively describes the relationship between the hysteresis and the sliding angle:

$$mg\left(\sin\alpha\right)/w = \gamma_{LV}\left(\cos\theta_R - \cos\theta_A\right) \tag{6}$$

where θ_A and θ_R are the advancing and receding CAs, respectively (Figure 2), g is the gravitational force, m is the mass, and w is the width of the droplet.

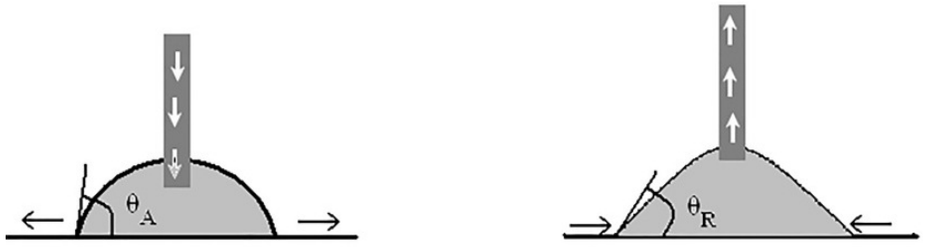

Figure 2. Illustration of the advancing and receding CAs.

Advancing and receding CA represent the maximum and minimum values that can be measured on the surface for the static CA. Due to the increasing interest on smart materials (self-cleaning and superhydrophobic), the dynamic CAs and CA hysteresis are highly applied [46, 47]. For self-cleaning applications, it is important that sliding angles (angle of the substrate which has to be tilted in order to move the droplet) to present small values.

From Eq. (6), it can be inferred that a lower droplet mass and smaller difference between the advancing and receding CAs will result in a smaller angle α. It is worthy to note that the surface roughness has a strong effect on the CA hysteresis [43].

Zisman observed for the first time that $\cos\theta$ increases linearly as the surface tension of the liquid (γ_{LV}) decreases [48, 49]. He investigated the wettability of solids by determining the

critical surface tension using CA. This method is used to determine the so-called critical surface free energy (γ_c), that differs from the solid surface free energy, γ_S. According to his method, the value of γ_C of a solid is equal to the value of γ_L of a liquid, which is in contact with the solid and for which the CA is zero. The value for γ_c is determined from empirical investigations, consisting of the CA measurements for the studied solid and the liquids of a homologous series of organic compounds like *n*-alkanes. The values are plotted with the *y*-axis corresponding to the cosine values of the CA (θ) and the *x*-axis relating to the γ_L values for the studied liquids. The values of $\cos\theta$ for the liquids of a series of *n*-alkanes form approximately a straight line. Extrapolation of this line to the point of $\cos\theta = 1$ yields the value of γ_C equal to γ_L.

Despite the fact that γ_C is not the solid surface free energy, the critical surface tension has been shown to correlate with the known surface chemistry of several solids.

The Zisman method has been widely used to assess the critical surface tension γ_C of different organic films or low-energy solids deposited on high-energy solids (e.g., metals, glass [50, 51]). In this approach, by using series of homologous nonpolar liquids (e.g., *n*-alkanes), one can obtain the total solid surface energy of a nonpolar solid and the dispersion component (γ_S^d) of the total surface energy of a polar solid. We note that, when using polar liquids on polar and nonpolar solids, one can obtain the deviation from rectilinear relation. Also by using polar liquids, the determination of any component of the solid free energy it is not possible.

2. Alternative deposition techniques employed for the synthesis of hydrophobic/hydrophilic nanostructured surfaces (thin films or nanoparticles)

Many methods were employed to synthesize hydrophobic or hydrophilic nanostructures (thin films, TFs, and nanoparticles, NPs), and some literature examples limited to ZnO, SiO_x, TiO_2, and DLC are summarized in Table 2.

Among these methods, pulsed laser deposition (PLD), sol-gel (SG), thermal evaporation (TE), solution based on chemical approaches, sputtering, and plasma enhanced chemical vapor deposition (PECVD) will be briefly described hereinafter. They are easy to use, low cost, and yield high throughput of micro- and nanostructures.

Material	Structure type	Deposition technique	Cited reference
ZnO	TFs	SG	[52]
	TFs	Metal-organic vapor deposition	[53]
	NPs	Microwave plasma	[54]
	TFs	Magnetron sputtering, MS	[55]
	TFs	Electrodeposition	[56]

Material	Structure type	Deposition technique	Cited reference
	TFs	Atomic layer deposition	[57]
	TFs	Electrochemical anodization	[58]
	TFs	PLD	[59]
SiO_x	TFs	Sputtering	[60]
	TFs	Ion beam evaporation, IBE	[61]
	TFs	PECVD	[62–64]
	NPs	SG	[65, 66]
TiO_2	NPs	IBE	[67]
	TFs	PECVD	[68, 69]
	TFs	Sputtering	[70, 71]
	NPs	(Dip-)pad-dry-cure	[72, 73]
	NPs	Impregnating TiO_2 particles in a resin and this composite deposited into the yarn-array	[74]
	NPs	SG	[75, 76]
	TFs	PLD	[77, 78]
DLC	TFs	PECVD	[79–81]
	TFs	MS	[82, 83]
	TFs	Combined PECVD and MS	[84]
	TFs	Filtered pulsed arc discharge	[85, 86]
	TFs	Ion beam deposition	[87]
	TFs	PLD	[88, 89]

Table 2. Different deposition techniques used for the synthesis of hydrophobic/hydrophilic ZnO, SiO_x, TiO_2, and DLC nanostructures.

In the field of TFs growth, PLD has proven to be among the most versatile methods [59], with features superior to conventional deposition techniques (fast processing, reliability and low production cost). In this technique, high power laser energies are used. They are focused onto a target in order to evaporate its surface under vacuum or different gas ambient atmospheres. The vaporized material consisting of ions, atoms, or molecules is subsequently deposited onto a generally parallel substrate. Repeated laser pulses will result in the deposition of the TFs in form of a coating on the substrate.

One important advantage of PLD method is the stoichiometric transfer of different materials from the targets in the deposited films [59, 90, 91]. This represents a direct consequence of the high ablation rate that allows all elements to evaporate simultaneously [92]. This technique ensures an excellent adherence of the deposited structure to substrates, the high accuracy control of the growth rate (10^{-2}–10^{-1} Å/pulse), the absence of contamination, the simplified growth of materials and combinations of materials of technological interest [93], and the good control of the final crystalline state of the coatings [59, 94].

The SG process is a synthesis route consisting in the preparation of a sol and successive gelation and solvent removal. This technique represents one of the simplest approaches to produce TFs. It presents many advantages in comparison with traditional deposition techniques, such as low working temperature, possibility to cover large surfaces, and high purity of the working conditions.

Compared to the physical route where harsh conditions such as high temperature or special equipment are usually required and consequently generating high costs, the solution based on chemical approaches [95–97] presents several advantages, including the simplicity in operation, low fabrication costs, low process temperatures (below 90 °C), and ambient pressure processing.

Thermal vacuum deposition or TE method is used to fabricate TFs under a high vacuum environment. In this method, an electron beam (e-beam) or resistive heating is usually used to evaporate the desired material inside the vacuum chamber, which then adheres to a substrate positioned above it.

The uniformity, high quality, and adherence of the deposited materials on large areas; the high deposition rate; and the versatility of sputtering techniques have made them attractive for the production of TFs [98–101]. In plasma sputtering deposition, plasma is used as the source of ions. These ions bombard a solid material, commonly known as the cathode or the target, with a typical kinetic energy of several hundreds electron volts. The ion bombardment produces the emission and acceleration of the secondary electrons, which play an important role in maintaining the plasma around the cathode [102]. The ionizing energetic electrons are confined close to the cathode allowing operation at high plasma densities and low pressures.

3. Synthesis of hydrophobic/hydrophilic oxides and DLC nanostructures onto textiles and metallic medical substrates

A brief literature review on results regarding oxide (ZnO, TiO_2, SiO_x) and DLC nanostructures synthesized by PLD, SG, TE, solution based on chemical approaches, sputtering, and PECVD onto textile or metallic substrates will be presented hereinafter. Polyester, cotton/polyester, and poly(lactic acid) woven fabrics can be coated with multifunctional oxide materials in form of TFs or NPs to get properties that increase the protection and comfort of the wearer. When covering the surface with NPs, a new roughness is added leading thus to a dual-size surface roughness. Therefore, the study of wettability properties is a tool to test the surface functionalization [103]. It is well known that wetting of a surface by a liquid is affected by surface roughness [104]. In the case of textile materials, the roughness is related to the geometry which is very complex [105]. Due to the fiber topography, the construction of the yarn, and the construction of the fabric, polymer, natural, and synthetic fibers might be made from porous materials that can absorb water from the environment. Fabrics have thus pronounced texture, porosity, and also (oriented) in-plane capillarity along the threads [103]. CAs on textile substrates can be useful quantities for comparative measurements in order to characterize the effects of surface modification, especially if the textile is distinctly hydrophobic [105]. Titanium

(Ti) stands for the most used metallic material for medical applications due to its unique properties such as biocompatibility, excellent mechanical properties in bulk, relative to the low mass density, and high corrosion and ductility resistance [106].

3.1. ZnO

ZnO is an *n*-type metal oxide semiconductor having a wide band gap, high electron mobility, and thermal conductivity. It mainly crystallizes in the wurtzite phase, being intrinsically polar, and thus exhibiting interesting piezoelectric properties. In addition, in the form of TFs or NPs, ZnO possesses promising antibacterial and antifungal, photocatalytic, electrical, electronic, and optical properties [107–115]. Recently, combinations ZnO-organic were tested for various applications requiring antimicrobial properties [116, 117]. Also, ZnO has probably the richest family of structures' morphology including rods, prisms, wires, whiskers, or tubes [95–97, 118–123]. Moreover, morphology influences other properties such as wettability, another significant characteristic of ZnO covered surfaces bringing great advantages in a wide variety of applications in industry and daily life [124–127]. For example, wettability is critical in cosmetics and textile fields where ZnO can be used due to its biocompatibility property.

Hydrophobins are a class of small-size cysteine-rich proteins synthesized by filamentous fungi [128]. They form ~5–10 nm thick self-assembled monolayers [129] on different substrates, changing their surface wetting properties. Namely, hydrophobic surfaces can be turned to hydrophilic, while hydrophilic materials become hydrophobic [130] after immersion in an aqueous solution of hydrophobin. Textile materials can be finished with various functionalization agents, such as chitosan microcomposites [131] or nanocomposites [132, 133], medicinal herbs [134], nisin [135], polyhexamethylene biguanide [136], or PMMA nanocomposites [137], in order to obtain new surface properties like antimicrobial, hydrophobicity, resistance to laundering, or protection against decoloration. Due to exceptional surface properties and to the tuning opportunities, their use is envisaged in cosmetic industry, polymer emulsion synthesis, and biosensing [138].

3.1.1. ZnO nanostructures synthesized by PLD onto cotton/polyester textiles

Yang et al. [139] and Papadopoulou et al. [140] demonstrated that the structures synthesized by PLD can be controlled in terms of wetting behavior. Therefore, ZnO structures showed a hydrophilic behavior after exposure to UV and were converted to hydrophobic after thermal treatment or storage in complete darkness. In this respect, a one-step PLD procedure to obtain either hydrophobic or hydrophilic ZnO structures (TFs or NPs), without any complementary post-deposition treatments of the surface, was recently proposed [141]. Depending on the number of applied laser pulses, well-separated NPs (for 10 pulses) or compact TFs (for 100 pulses) were synthesized. By varying the ambient gas nature and pressure inside reaction chamber, hydrophilic or hydrophobic surfaces were obtained. The expected properties of the textiles coated with ZnO were evaluated at room temperature (RT) by static CA measurements.

The TFs deposited on textiles (Figure 3) in a flux of 13 Pa oxygen were highly transparent and had a hydrophilic behavior (Figure 3a), while those obtained in vacuum were opaque and showed a hydrophobic behavior (Figure 3b).

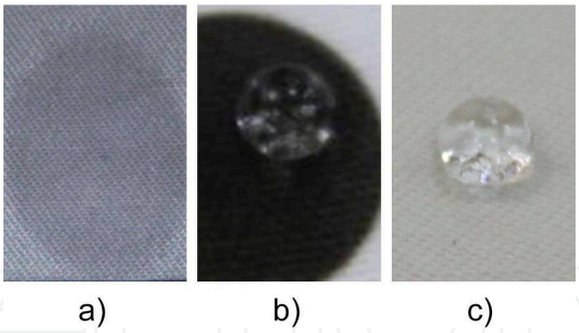

Figure 3. Textiles coated with ZnO nanostructures: (a) hydrophilic TF deposited in 13 Pa oxygen, (b) hydrophobic TF deposited in vacuum, and (c) hydrophobic NPs deposited in vacuum.

A CA of 157° (Figure 4) was measured, which qualified these films as superhydrophobic.

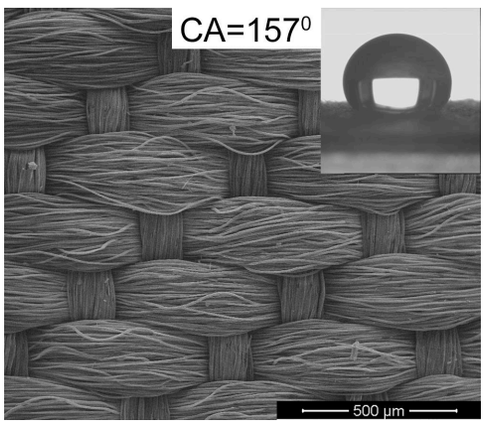

Figure 4. SEM micrograph of the superhydrophobic textile coated with ZnO TF in vacuum. Inset: water droplet in static mode with the CA of 157°.

In the case of NP samples, eye examination confirmed a hydrophilic behavior for the structures deposited in the oxygen flux and a hydrophobic one after deposition in vacuum (Figure 3c).

The macroscopic and microscopic observations have revealed a smoother surface in case of TFs deposited in vacuum characterized by a six times smaller RMS and negative values for surface skewness (S_{sk}) and kurtosis (S_{ku}) (Table 3).

Amplitude parameters	**Sample type/scanning area**			
	TFs oxygen/10×10 µm²	TFs oxygen/2×2 µm²	TFs vacuum/10×10 µm²	TFs vacuum/2×2 µm²
RMS (nm)	36.817	36.793	6.578	5.796
S_{sk}	0.404	0.421	–0.113	–0.0731
S_{ku}	0.0274	0.24	–0.375	–0.357

Table 3. Amplitude parameters for ZnO TFs deposited in 13 Pa oxygen flux and vacuum. Reproduced from Popescu et al. [141].

http://dx.doi.org/10.5772/60808

Figure 5 shows two-dimensional AFM images of the TFs deposited in 13 Pa oxygen flux and vacuum. The grains (of ~140 nm) visualized by AFM (Figure 5b, d) were in fact consisting of very small crystallites (of ≤10 nm), as proved by the XRD patterns.

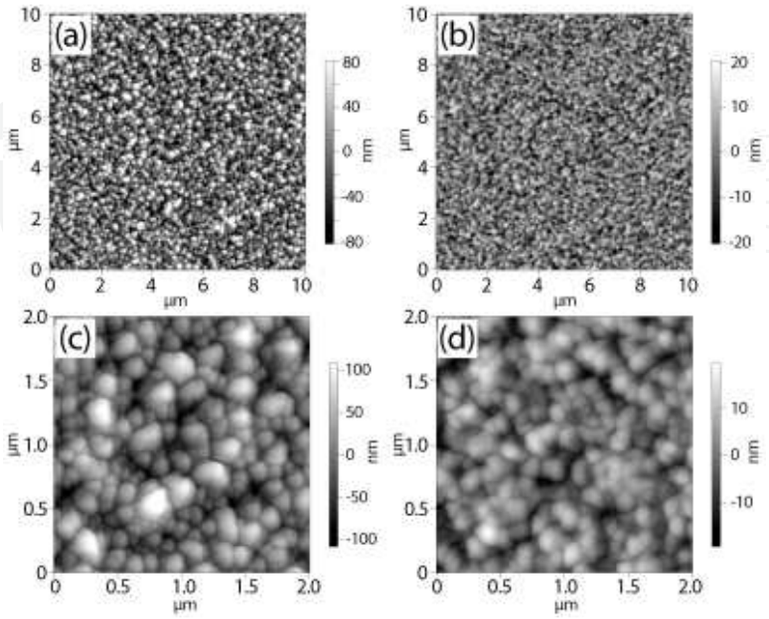

Figure 5. Two-dimensional AFM topography images of the TFs deposited in (a, c) a 13-Pa oxygen flux and (b, d) vacuum at different scales: (a, b) (10 × 10) μm² and (c, d) (2 × 2) μm². Reproduced from Popescu et al. [141].

In order to account for the significant difference observed in the wetting behavior of the TFs and NPs deposited in a flux of oxygen and in vacuum, a model was proposed for surface wetting. The numerous gaps between crystallites are filled with air acting as a support "buffer" for the water droplet, in contact to the surface in a few small nanometric sites only. Conversely, the TFs deposited in an oxygen flux (Figure 5a, c) consist of larger crystallites and a few intergranular pores only. Thus, the air "buffer" is rarefied, so the contact between the water droplet and the ZnO surface is extending over a larger area (Figure 6). The droplet weight prevails over the counter pressure exerted by the ZnO surface and eventually collapses under its own weight. Figure 6 shows schematically the water droplet in contact with ZnO structures synthesized in vacuum (Figure 6a) and oxygen flux (Figure 6b).

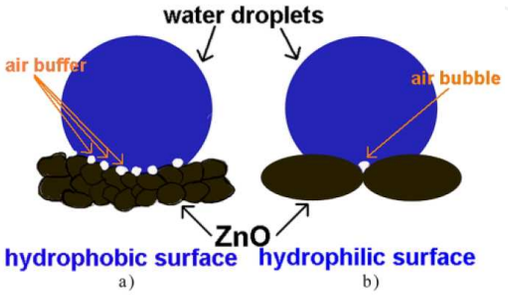

Figure 6. Schematic of the water droplet in contact with ZnO surface deposited in (a) vacuum and (b) 13 Pa oxygen flux. Reproduced from Popescu et al. [141].

The NP depositions in vacuum consist of a large number of small crystallites, which include a huge amount of vapor pockets. Their action cumulates with the effect of the air, which is present in the space between NPs to more efficiently support the droplet weight. This model is in accordance with other studies on hydrophobic plant leaf surfaces [142]. Accordingly, the largest contact area between the water droplet and the leaf surface corresponds to flat and microstructured surfaces but is generated in case of nanostructures as an effect of vapor pockets entrapment.

The electric charging of the surface should be considered when explaining the affinity or repellency to water of ZnO structures. XRD investigations demonstrated that the ambience in the interaction chamber also showed the combinations between Zn and O atoms in the crystalline lattice [141]. In case of structures deposited in vacuum, there is a mix in each crystalline plane of positive and negative charges. One should note that the water droplet is neutral from the electrical point of view. Accordingly, the deposited structures do not interact electrically with the water droplet. Oppositely, the structures deposited in an oxygen flux have only one type of atoms per plane that induce a positive (Zn) or negative (O) charging of surface [141]. The synthesized structures interact electrically with the droplet to reach the neutral status, thus attracting the water bubble toward the ZnO surface causing supplementary stress that contributes to the collapse of the bubble.

In a parallel study, the capacity of these oxide nanostructures to completely inhibit fungal development and neutralize bacteria was found to be a direct consequence of their wetting behavior [1-6].

The intercalation of a hydrophobin nanolayer between substrate and ZnO film, which can boost the oxide efficiency against microorganisms with a higher natural resistance, was recently studied and an explanation of the observed phenomena was proposed [143]. In case of ZnO TFs deposited on bare textiles, the adhesion is governed by physical mechanisms only (as e.g., mechanical or dispersion adhesion [144]), while in case of a buffer layer of hydrophobin interposed between textile and ZnO, chemical bonding occurs, the fastening between the ZnO and the textile substrate becoming much stronger. When used alone, the hydrophobin had no effect on both *Candida albicans* colonies and six strains of filamentous fungi. In case of simple finishing with ZnO, the reduction rate was of 50% and 70% of the colonies in 24 h (Figure 7a, b).

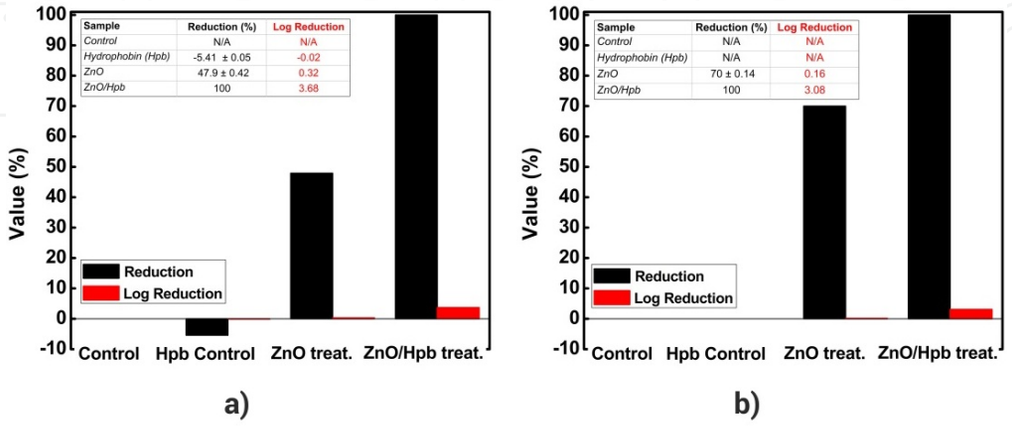

Figure 7. Percentage and logarithmic reduction of (a) *C. albicans* population and (b) mold mix inoculum after 24 h cultivation on untreated and ZnO treated textiles. Reproduced from Popescu et al. [143].

http://dx.doi.org/10.5772/60808

In order to improve ZnO efficiency against resistant fungi, the oxygen concentration on films' surface was increased by covering the textile fibers with hydrophobin and then adding an upper layer of ZnO. As an effect, the orientation and shape of ZnO crystallites were changed, the (001) film texturing becoming more pronounced and nanocrystallites elongated, with more polar planes (001) parallel to the surface (Figure 8a). Depending on the orientation of the *c*-axis, these planes may contain oxygen atoms only (Figure 8b). The ZnO film deposited on hydrophobin proved in this case 100% efficient in reducing colonies of both *C. albicans* and a mold mix of filamentous fungi (Figure 7a, b). This significant enhancement was attributed to the higher texturing of the oxide film when growing on hydrophobin interlayer, resulting in an increased presence of oxygen species on surface.

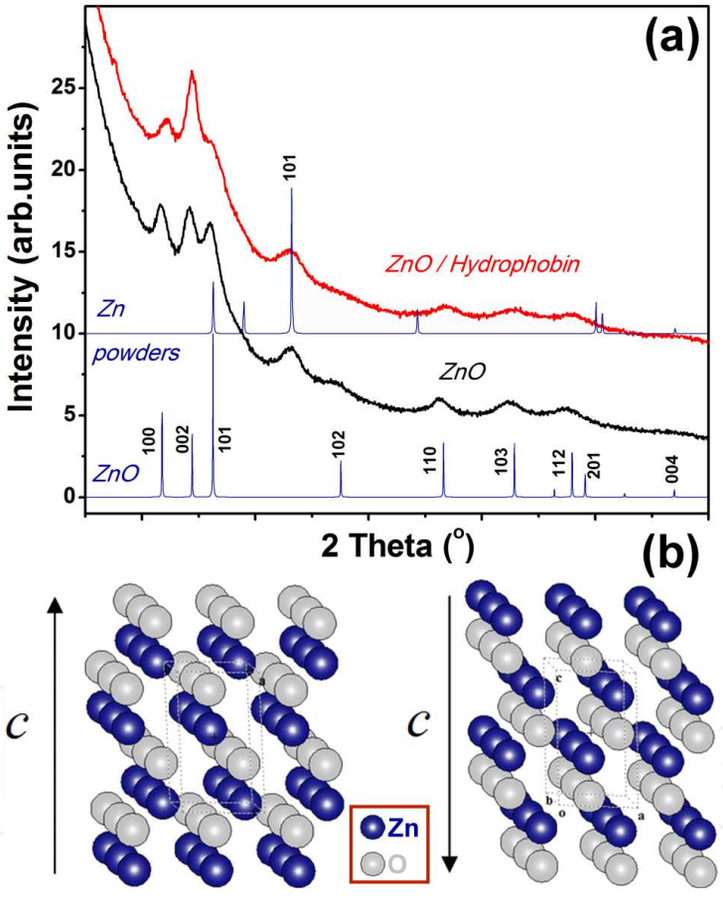

Figure 8. XRD patterns of ZnO TFs (a); the orientation of the (001) ZnO crystallites grown on hydrophobin, resulting in outer termination either in O or in Zn atoms only (b). Reproduced from Popescu et al. [143].

ZnO is recognized to possess antibacterial and antifungal properties. Nair et al. [109] assessed the microbiological activity of ZnO against a mold mix of microbes and associated the high reduction ratio to the generation of surface oxygen species. Sawai et al. [110] and Premanathan et al. [111] suggested that these oxide species form in wet media hydroxyl radicals and hydrogen peroxide. As known, the hydroxyl radical is the most reactive one, able to interact

with almost every type of molecule of the living cells of bacteria and fungi, causing irreversible damage to cellular components and eventual apoptosis. Applerot et al. [112] advanced a mechanism for the reactive oxygen species formation on ZnO surface. The oxygen atoms present on surface interact with water molecules, forming OH^- radicals. A chain reaction occurs, resulting in exponential multiplication of these radicals on surface.

We note that no negative side effects of hydrophobins when in contact with human tissue were reported [145], and to the benefit of biomedical applications, they were able to form, in specific cases, resistant monolayers with antimicrobial activity [146]. Moreover, the proposed antimicrobial finishing procedure of fabrics with a conjunction of a thin layer of hydrophobin and a ZnO layer can find applications in the medical field, where solutions are constantly required for elimination of microbial contamination, thus reducing the risks of infections during surgery.

3.1.2. ZnO nanostructures synthesized by solution based on chemical approaches onto solid (glass) substrates

In the synthesis process of ZnO nanostructures using solution based on chemical approaches, a zinc salt and a basic compound are brought together. The involved chemical reactions can be described as follows:

i. Using a weak base ($(CH_2)_6N_4$)

$$Zn(NO_3)_2 \rightarrow Zn^{2+} + 2NO_3^-$$
$$(CH_2)_6N_4 + 6H_2O \rightarrow 6HCHO + 4NH_3$$
$$NH_3 + H_2O \rightarrow NH_4^+ + HO^-$$
$$Zn^{2+} + 3NH_4^+ \rightarrow \left[Zn(NH_3)_4\right]^{2+}$$
$$\left[Zn(NH_3)_4\right]^{2+} + HO^- \rightarrow Zn(OH)_2 + 4NH_3$$
$$Zn(OH)_2 \rightarrow ZnO\downarrow + H_2O$$

ii. Using a strong base (NaOH)

$$Zn(NO_3)_2 \rightarrow Zn^{2+} + 2NO_3^-$$
$$Zn^{2+} + 2HO^- \rightarrow Zn(OH)_2$$
$$Zn(OH)_2 + 2HO^- \rightarrow \left[Zn(OH)_4\right]^{2-}$$
$$\left[Zn(OH)_4\right]^{2-} \rightarrow ZnO\downarrow + 2HO^- + H_2O$$

iii. Using a reducing agent ($(CH_3)_2NHBH_3$) [147]

http://dx.doi.org/10.5772/60808

$$Zn(NO_3)_2 \rightarrow Zn^{2+} + 2NO_3^-$$
$$(CH_3)_2NHBH_3 + 2H_2O \rightarrow HBO_2 + (CH_3)_2NH_2^+ + 5H^+ + 6e^-$$
$$NO_3^- + H_2O + 2e^- \rightarrow NO_2^- + 2HO^-$$
$$Zn^{2+} + 2HO^- \rightarrow Zn(OH)_2$$
$$Zn(OH)_2 \rightarrow ZnO\downarrow + H_2O$$

The ZnO structures were examined by XRD (Figure 9). The diffraction peaks observed at 2θ = (31.8°, 34.5°, 36.3°, 47.5°, 56.6°, 63.0°, 66.4°, 68.0°, and 69.1°) are characteristic to ZnO hexagonal wurtzite phase (JCPDS file no. 36-1451), with corresponding Miller indexes at (100), (002), (101), (102), (110), (103), (200), (112), and (201). The strong and sharp diffraction patterns suggest that the as-obtained structures are well crystallized.

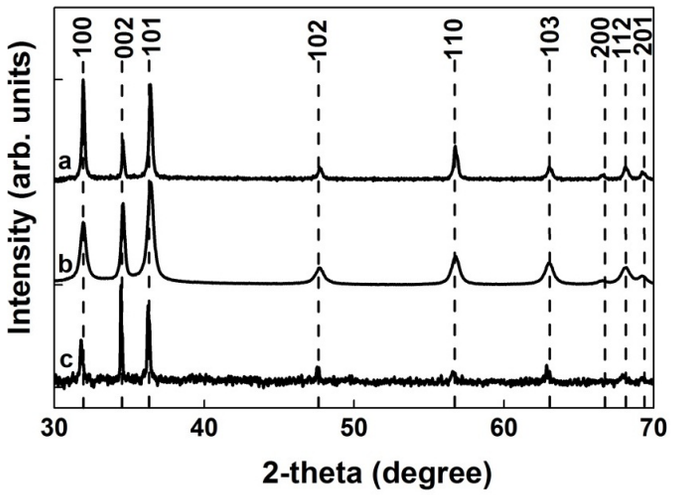

Figure 9. XRD patterns of ZnO samples synthesized in the presence of (a) $(CH_2)_6N_4$, (b) NaOH, and (c) $(CH_3)_2NHBH_3$.

SEM images of the samples (Figure 10) revealed the following morphologies for the ZnO micro/nanostructured TFs: rods (4.5 μm in length and 330 nm in diameter; Figure 10a, b), flowers (1–2 μm in dimension; Figure 10c, d), and hexagonal prisms (400 nm in length and 200 nm in diameter; Figure 10e, f). Insets to Figure 10 show the influence of the ZnO surface morphology on wetting behavior. The corresponding CA values of the ZnO samples are 164.8° (rods), 94.3° (flowers), and 79.4° (prisms). An explanation for the different values of CA can be related to the numerous gaps between the ZnO structures filled with air. For this reason, the film containing a higher volume of air trapped between the ZnO structures at the solid/water interface has a superhydrophobic behavior. The CA results were confirmed by AFM measurements (Figure 11). The RMS values were as follows: 390 nm (rods), 120 nm (flowers), and 50 nm (prisms).

Due to their morphology, the ZnO structures present different degrees of compactness, trapping more or less air in-between. In this way, the CA value is linked to the RMS value of the sample.

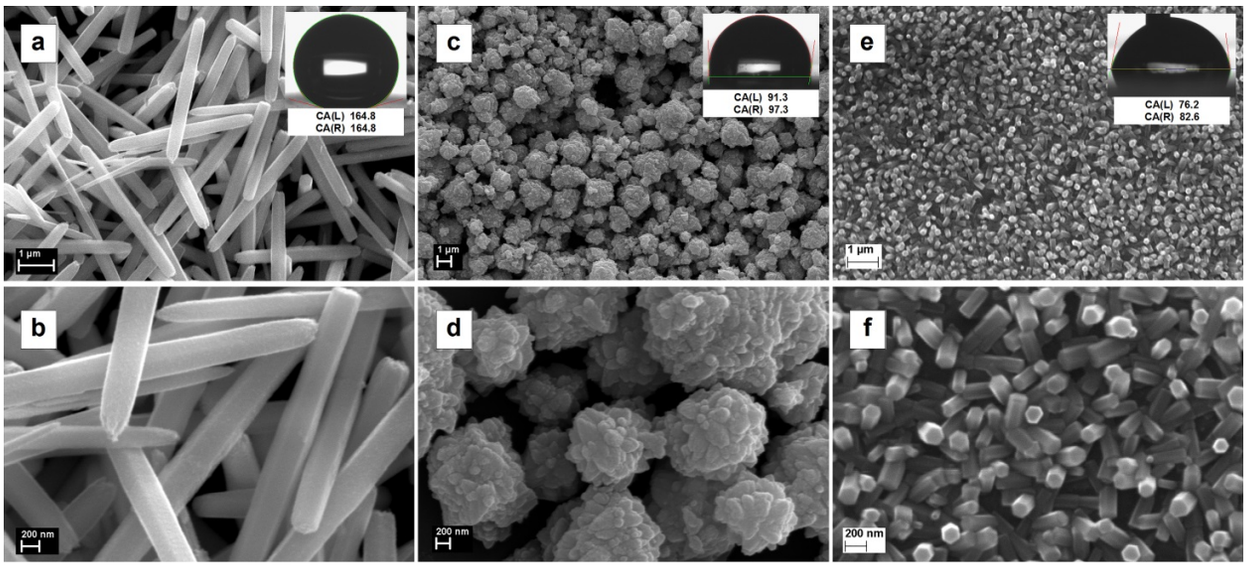

Figure 10. SEM images, at different magnification, of the ZnO samples synthesized in the presence of (a, b) $(CH_2)_6N_4$, (c, d) NaOH, and (e, f) $(CH_3)_2NHBH_3$. Insets: optical photographs of the water droplets shape on the ZnO surfaces with the corresponding CA values.

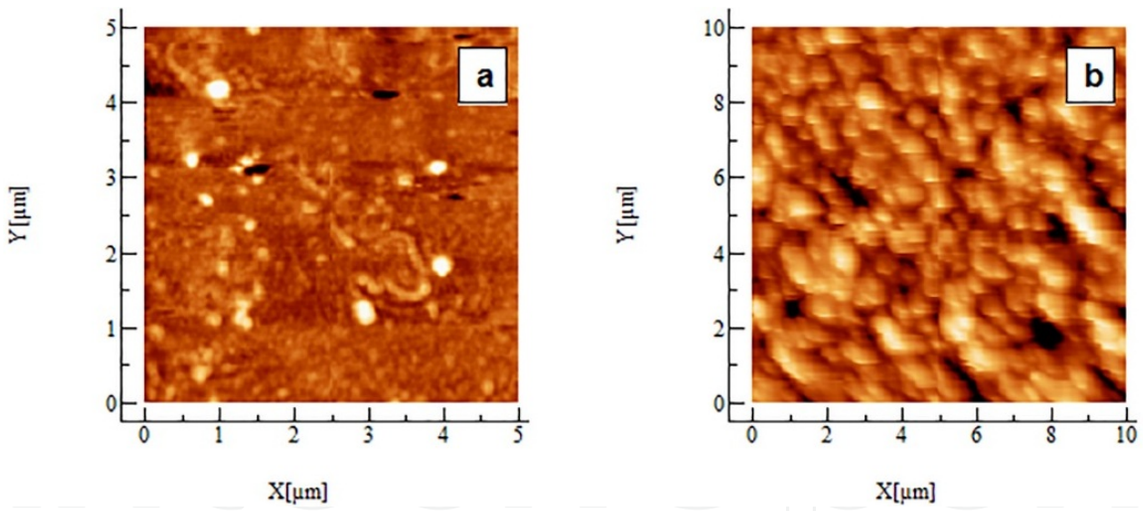

Figure 11. AFM images of the ZnO samples synthesized in the presence of (a) NaOH and (b) $(CH_3)_2NHBH_3$.

3.2. TiO_2

Titanium dioxide (TiO_2) is a transition metal oxide with UV absorbing properties with many technological applications [148, 149]. High photocatalytic efficiency, great stability, and low cost of production are in favor of TiO_2's photocatalytic properties [149]. In addition to bulk applications, TiO_2 TFs were obtained for UV blocking, antibacterial or/and photocatalytic properties [149].

3.2.1. TiO_2 structures synthesized by SG and sputtering onto textile substrates

Some properties of the substrates used in the experiments are summarized in Table 4.

Sample code	Textile 2D element/thread	Nature of fibers	Color	Thickness (mm)	Density (g/cm³)
P2	Knitted/interlock/Nm 70/1	Polyester	White	0.82	0.25
P3	Knitted/interlock/Nm 50/1			0.89	0.26
P28	Fabric			0.46	0.47
P30	Fabric			0.52	0.41
PLA	Nonwoven	Poly(lactic acid)		0.64	0.31

Table 4. Characteristics of different textiles functionalized with TiO_2.

XRD and SEM investigations [103] indicated, for both deposition techniques, that TiO_2 NPs were amorphous. Sputtered layers consisted of aggregates randomly distributed on substrate, while the SG layers showed a uniform distribution of NPs, with a mosaic-like structure. SEM images (Figure 12) suggest the formation of NPs, which are not singularly distinguishable. The sputtered layers consist of NP aggregates (in coalescence) with less than 20 nm diameter, randomly scattered on substrate. In the case of the SG layer, there are bridge-aggregated NPs leading both to a mosaic-like structure and to cracks and interfiber bonds [150].

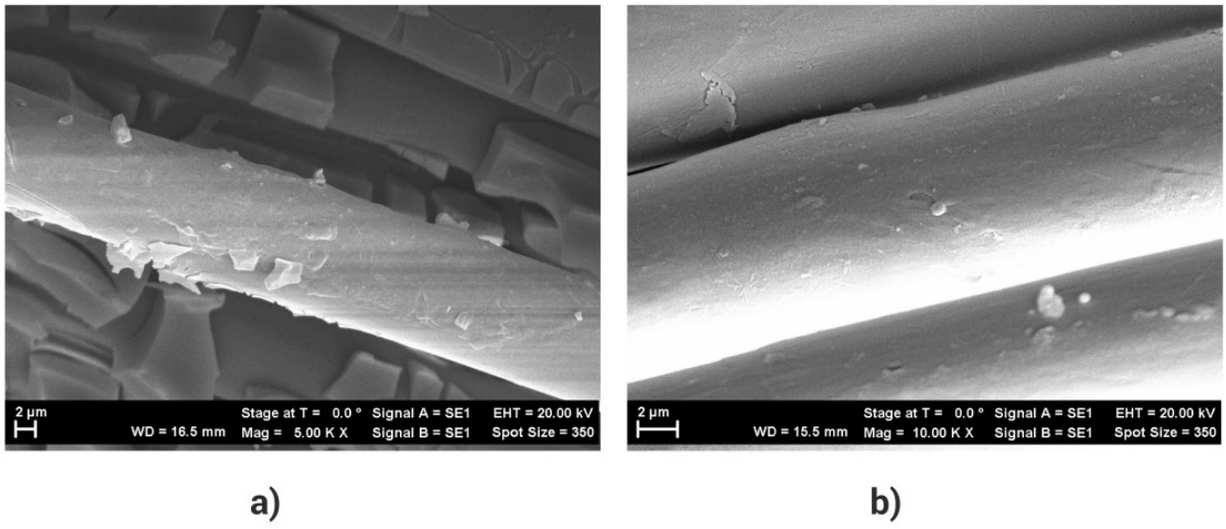

Figure 12. SEM images of TiO_2 samples deposited on P2 substrates by (a) SG and (b) sputtering.

A highly polar liquid–water was recommended [151] as testing liquid in CA measurements, for estimating the wettability of polar solids as polyester materials. The water repellency was thus regarded as indicating the performances of the coated layers and was evaluated by measuring static (equilibrium) CAs at RT [152]. In order to have a general

idea of the samples' wetting behavior, different measurement points on each sample were thus considered (Figure 13).

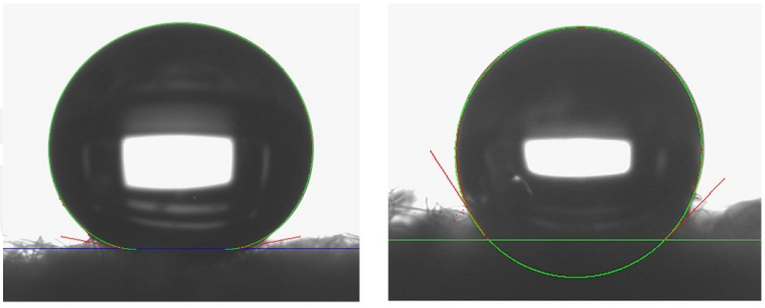

a) b)

Figure 13. Water droplets on TiO_2 deposited on P2 samples by (a) SG and (b) sputtering.

The mean CA values of the raw or coated samples are summarized in Table 5.

Sample code	CA (°)	$f = \frac{1+\cos\theta_c}{1+\cos\theta_0}$ *
P2	136.9	0.244
P3	138.1	0.231
P28	152.1	0.105
P30	124.8	0.389
PLA	129.6	0.328
TiO_2 SG/P2	169.3	0.017
TiO_2 SG/P3	169.7	0.016
TiO_2 SG/P28	152.7	0.110
TiO_2 SG/P30	158.9	0.067
TiO_2 SG/PLA	140.6	0.225
TiO_2 SP4/P2	133.8	0.209
TiO_2 SP4/P3	166.0	0.020
TiO_2 SP4/P28	Hydrophilic	0.681
TiO_2 SP4/P30	155.8	0.059
TiO_2 SP4/PLA	150.3	0.089

* θ_0 = 84° (for raw), 89.4° (for SG), and 62.1° (for sputtered) samples.

Table 5. Water CA values measured onto different investigated surfaces.

From Table 5, one can see that the CAs increase more by fabric modification (after Titania deposition). CAs were influenced by air, water droplet, and surface of fabric, which formed a nanorough substrate. One sample (P28) is hydrophilic meaning that water passes through it; this sample has voids large enough, and the margins become hydrophilic by deposition of hydrophilic particles. The behavior might be approximated by the Cassie–Baxter equation:

$$\cos\theta_c = f\cos\theta_0 - (1-f) \tag{7}$$

Here, θ_C is the composite CA formed on the treated fabric and θ_0 is the CA formed on untreated fabric [153]. The parameter f represents the fraction of the surface in contact with the water droplet. Knowing the corresponding CAs, its values can be calculated for each raw-treated pair of samples, using the following equation:

$$f = (1+\cos\theta_c)/(1+\cos\theta_0) \tag{8}$$

These values are summarized in Table 5. However, it seems that Cassie–Baxter equation (or Wenzel equation) should be applied to superhydrophobic surfaces with caution [154]. TiO_2 can be used to obtain hydrophobic surfaces by producing artificial roughness via micro structuring [155].

3.3. SiO_x

Silicon oxide was deposited onto polymeric substrates as a viable alternative to metallic depositions used for packing materials due to their transparency, recyclability, microwave use, and impressive barrier properties [156], to produce textiles with hydrophobic properties [157]. In addition, silica NPs immobilized on textiles can lead to flame retardant properties [158]. SG-deposited layer can be compared to the one deposited in vacuum at low angle because in both cases the deposit is awaited (super) hydrophilization evidence since SiO_2 brings its OH groups which print to the media hydrophilic properties. However, due to the columnary nanostructured relief of deposited layer, it was expected that the roughness of the textile surface would be increased. In addition, information was acquired on vacuum deposition at small angle [159–162]. Thus, we preferred this technique for a SiO_x deposition onto textile materials [163].

3.3.1. SiO_x structures synthesized by thermal evaporation at small angles onto polyester (P), polyamide (PA), poly(lactic acid) (PLA), and natural cellulosic hemp (H) substrates

The differences between the investigated textiles [163] are summarized in Table 6.

Sample code	Textile 2D element/thread	Nature of the fibers	Color	CA (°)	
				Raw textile	SiO_x/textile
P1	Knitted/interlock/Nm 70/1	Polyester	White	136.9	139.2
P2	Knitted/interlock/Nm 50/1			138.1	128.9
P3	Knitted/glat/Nm 50/1			158.2	154.9
P4	Fabric/Nm 70/2 + Nm 40/2			136.9	139.2
P27	Fabric			Hydrophilic	Hydrophilic
P28	Fabric			152.1	105.3
P30	Fabric			124.8	75.5
PA	Knitted	Polyamide		165.1	97.6
PLA	Nonwoven	Poly(lactic acid)		129.6	Hydrophilic
H	Fabric	Hemp	Beige	126.9	135.0

Table 6. Different functionalized textiles and their corresponding static CA values.

The XRD diffractograms pointed to an amorphous phase of the SiO_x deposited layers [163].

SEM morphologies of SiO_x particles synthesized on fabrics are presented in Figure 14. The raw material images showed defects like kink bands, dislocations, nodes, and slip planes, which are common characteristics of hemp materials [164]. SEM images of synthesized samples showed that SiO_x particles were grown on the fiber surfaces in a continuous and noncolumnar layer (Figure 14). Apparently, each individual fiber of samples looks uniformly covered by an amorphous layer [163].

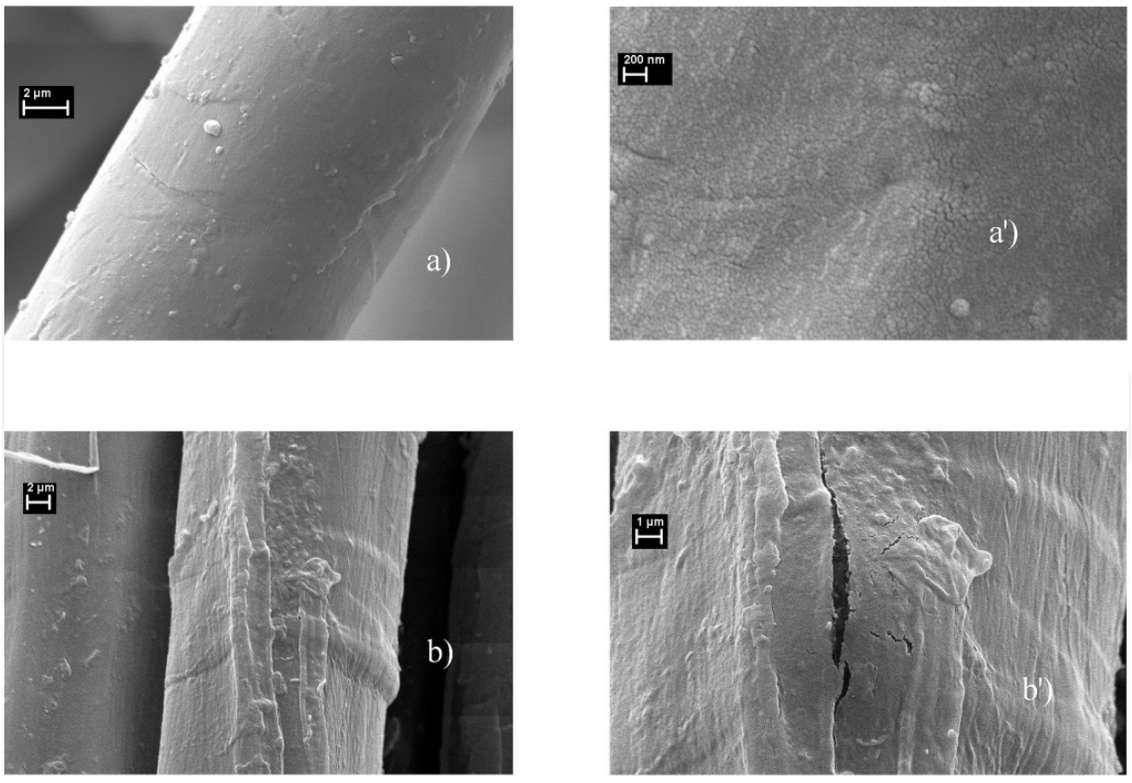

Figure 14. SEM images of SiO_x layers deposited on (a, a′) P2 and (b, b′) H substrates, at two different magnifications.

The wettability properties were evaluated by measuring static (equilibrium) CAs. The measurements were carried out at RT [152]. The images were processed using specific programs to fit the profile with the Young–Laplace equation in order to obtain the value of static CA.

In Figure 15, the image of the water droplet onto the deposited P2 sample and the corresponding CA is represented. The measurements were performed for a direction parallel to the privileged one of the knitted matter (vertically advance geometry). When following a direction perpendicular to the privileged one, the measurements evidence differences of few degrees only.

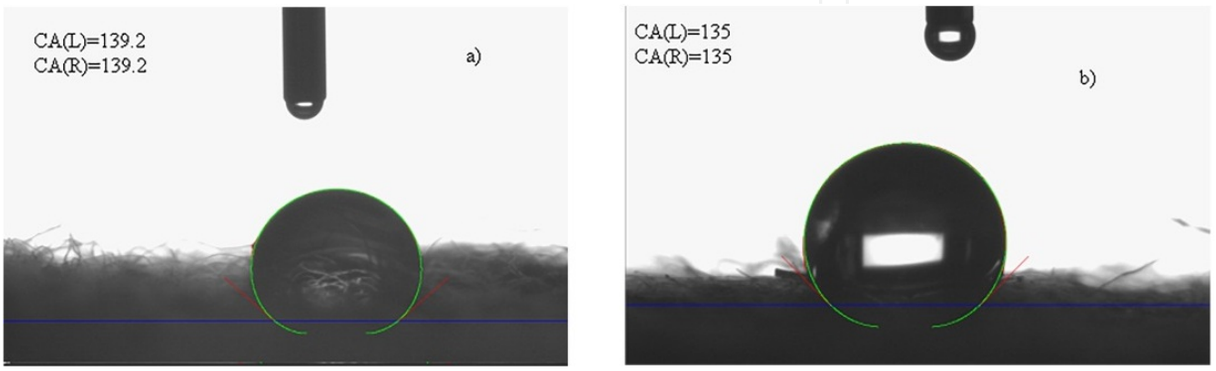

Figure 15. Water droplets on SiO_x TFs deposited on (a) P2 and (b) H samples. Reproduced from Frunza et al. [163].

From Figure 15, one can observe that the investigated surfaces are not flat, smooth, or homogeneous. These characteristics of the samples make it difficult to apply a specific model algorithm. Moreover, wetting of fabric surfaces is complicated by the heterogeneity, the diffusion of liquid into the fiber, and the capillary action of the fiber assembly. Under these conditions, the experimentally measured CA is an apparent one and can differ considerably from the actual value [163].

The mean CA values of the raw and deposited samples are summarized in Table 6. One can observe that the CA generally decreases after surface functionalization with SiO_x, in a range of few up to several tens of degrees. As expected, the presence of SiO_x NPs onto the fiber surface confers to the textiles a hydrophilic behavior (see Table 6).

3.3.2. Surface free energy of SiO_2 (quartz) inferred from CA measurements

Starting from known values of the dispersive and polar parts of the probe liquids' surface tension and obtained values of the CAs, the dispersive and polar parts of the surface tension of the solid (fused quartz) were estimated either by minimization of the equation system using the least square method or by solving the equations taken for combinations of two probe liquids [165].

Eq. (9) is a relation between the dispersive and polar parts of the solid substrate's surface tension and the same quantities of the surface tension of the wetting liquid and the corresponding CA:

$$\gamma_L(1+\cos\theta) = 2\sqrt{\gamma_S^d}\sqrt{\gamma_L^d} + 2\sqrt{\gamma_S^p}\sqrt{\gamma_L^p} \quad (9)$$

The values γ_S^d and γ_S^p were obtained by averaging the dispersive and polar components of γ_S resulted from solving Eq. (9) for all pairs of liquids that have the condition number of system matrix low enough (as defined in [166]).

CAs of water on fused silica can vary in a large interval. This behavior is in agreement with the one described in the literature, for example, with a 20º to 80º range obtained on quartz dehydroxylated by heating, slightly contaminated, or deliberately methylated [167]. The values we found can be interpreted in terms of the dependence of water CAs on sample purity; the presence of amorphous materials, chemicals, heating, and other pretreatments; and contamination by adsorption of substances from laboratory ambient. All these factors could have an influence over the increasing values of the CA. The obtained values were supposed to depend on the amounts of silanol groups and physically adsorbed water molecules on the quartz/silica surface. The investigation of "cleaner" surfaces obtained by a thermal treatment removing the hydroxyl groups at temperatures of the beginning and ending of the dehydroxylation process [168] was carried out.

The components of surface free energy of fused silica were determined by CA measurements of several liquids (see Table 7).

Treatment temperature (°C)	**CA for different liquids (°)**				
Water	Glycerol	NP5	Ethylene glycol	Dimethyl sulfoxide	
240	5.3	14.2	24.9	8.3	0
1000	33.6	14.8	24	0	6.5

Table 7. Values of CA (°) of different liquids on fused quartz treated at two different temperatures.

The fused silica plate samples were heated in atmosphere in order to remove water adsorbed on surface and most of the silanol groups. Measurements of CA on solid substrate were performed by analysis of the profile images of symmetric static liquid drops using the Drop Shape Analysis System (model DSA 100, from Krüss) [141, 152]. The samples were placed on a stage, under the tip of liquid-dispensing disposable blunt-end stainless steel needle with an outer diameter of 0.5 mm. The fixed needle was attached to a syringe pump, which was controlled by the computer for drop delivery. The volume of the drops was of ~ 2–3 μl. The CAs were determined by fitting the shape of the sessile drop with a smooth curve and then calculating the slope of the tangent to the drop at the liquid–solid–vapor interface. Low CAs ($\theta < 30º$) were determined by fitting the shape of the sessile drop with a circle, whereas larger CAs were estimated by fitting the drop shape with a polynomial equation of second degree or a circle equation. The camera was positioned to observe the droplet under an angle of about 2°–3° in respect to the sample surface supporting the droplet. The tests were carried out at RT.

CAs were obtained with an uncertainty of ±2° due to combined effects of drop asymmetry, surface heterogeneity, and variation in drop position on the plate.

Representative images of the observed water droplets on plates are given in Figure 16.

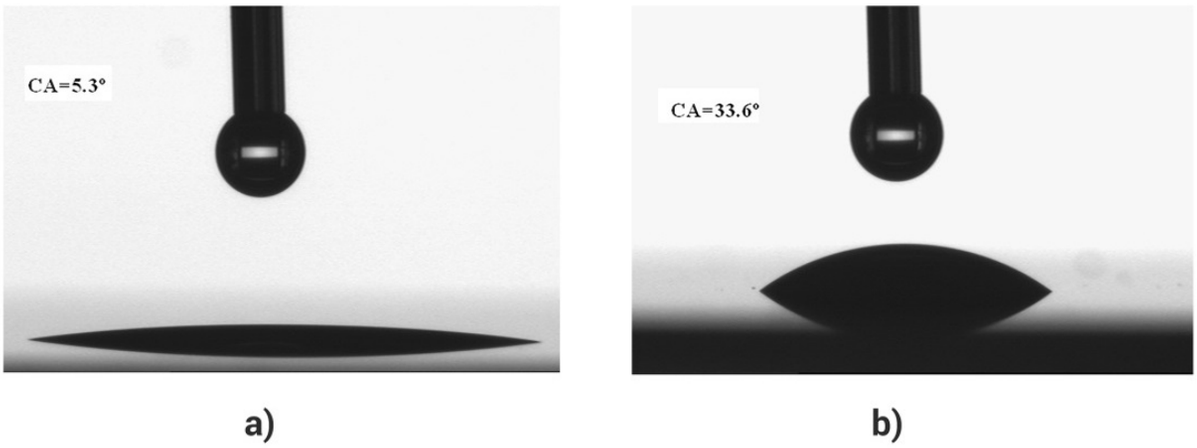

Figure 16. Water droplets on the SiO_x plates treated at (a) 240°C and (b) 1000°C, and the corresponding CAs.

Based on literature values [169–171] of the polar and dispersion parts of the liquid surface tension (see Table 8) and using the methods of geometric or harmonic mean for the interaction term, the calculation of the two components for fused silica (see Table 9) gave some differences, but their sum did not differ much. Moreover, our tests seem to indicate the method of harmonic mean as better than that one of Owens–Wendt [165].

Sample liquid	Dipole moment (D)	γ_L (mN/m)	γ_L^d (mN/m)	γ_L^p (mN/m)
Water	1.85	72.8	21.8	51.0
Glycerol	2.56	63.3	33.6	29.7
Ethylene glycol	2.69	48.0	33.8	14.2
Dimethyl sulfoxide	4.11	44.0	36.0	8.0
NP5	1.70	38.1	34.1	4.0

Table 8. Physical properties of different liquids used as samples.

Treatment temperature (°C)	Owens-Wendt/least squares (mN/m)		Owens-Wendt/ Average (mN/m)		Wu/ least squares (mN/m)	
	γ_s^d	γ_s^p	γ_s^d	γ_s^p	γ_s^d	γ_s^p
240	11.96	61.16	12.36	60.32	23.70	46.67
1000	15.96	46.90	15.96	49.56	25.29	37.48

Table 9. The surface tension components (dispersive γ_s^d and polar γ_s^p parts) of fused silica obtained by different calculation methods.

The polar part of the surface free energy of fused silica thermally treated is higher than the dispersive part as resulting from both methods (geometrical and harmonic mean). This might be an indication that, at the measurement moment, the plate surface was not (totally) covered by water vapors from environment.

In agreement with the decreasing number of silanol groups by the thermal treatment, the polar part of the surface tension shows a decreasing trend when increasing the pretreatment temperature.

The indirect method of CA measurements applied for the set of liquids chosen to have complementary interactions with quartz surface, allowed for obtaining values for the components of the surface free energy.

3.4. Effects of proteins from blood plasma on the hydrophobicity of DLC films

The amorphous phase of sp^3 bonded C atoms is known as DLC [82, 172, 173]. Beside high wear resistance coatings for metallic parts, DLC also proved useful in coating implants due to specific surface properties (low surface energy values and chemical inertness) that prevent blood coagulation and favor osteoblasts adhesion [90, 172]. In the biomedical field, the main necessity for DLC coatings comes from vascular prostheses. In the case of interaction with blood, it seems that DLC quality has a major influence upon clotting time. During the blood flow through these tubes, the erythrocytes and thrombocytes (platelets) aggregate in certain spots and may eventually block the blood passage. To compensate for this general weakness of vascular prostheses, DLC films can bind albumin molecules from the sanguine plasma forming a passive layer that makes the surfaces less adhesive for blood platelets [174].

The blood compatibility with carbon-based films is extremely complex and for the moment there is no relation found between hemocompatibility and surface properties such as surface energy, atomic bond structure of carbon, or composition of material. Contradictory data have been reported regarding the behavior of the material in terms of blood clotting, the adherence of platelets, or protein adsorption to surfaces. The relationship between the sp^3 bonds content of DLC and its antithrombogenicity properties is still not well understood. In vitro [82] and in vivo [88, 175] studies indicate that better results can be obtained for a higher sp^3 content.

Kwok et al. [176] pointed out that a higher surface energy of phosphorous doped a-C:H films is associated with a low adsorption of proteins, among them the albumin being the preferential one. Similar findings in terms of protein adsorption were presented by Ma et al. [177], who reported a higher albumin to fibrinogen adsorption ratios on surfaces with higher surface energy.

Jones et al. [178] explored platelet attachment on Ti, TiN, TiC, and DLC surfaces and reported that the more hydrophilic surfaces present a greater platelet spreading and fibrinogen adsorption. They suggested that the better hemocompatibility of DLC surface is linked to its low surface energy and thus high hydrophobicity. Okpalugo et al. [179] also noted that improved blood compatibility can be obtained when surface energy is lowered in silicon doped a-C:H films.

http://dx.doi.org/10.5772/60808

Recently, the correlation between activated partial thromboplastin time (aPTT) and surface energy of DLC structures with different sp^3/sp^2 bonds ratio was studied. Attention was paid to the investigation of protein adsorption and platelets adherence to the surface, both acting as crucial factors for material hemocompatibility [84].

3.4.1. Types of bonds in the films

XPS analysis, indicating the C 1s core level variation, was used in order to assess the amount of sp^2 and sp^3 bonded C in three types of samples (D20, D60, and D100; see Table 10).

Sample	Component (%)			sp^3/sp^2 ratio
	C=O/–COO	sp^2-C	sp^3-C	
D20	5.7±0.3	35.9±1.2	58.4±2.0	~1.6
D60	4.3±0.2	17.3±0.6	78.4±2.4	~4.5
D100	2.8±0.15	9.7±0.5	87.5±3.4	~9.0

Table 10. XPS peak separation data for the C 1s line of DLC films. Reproduced from Popa et al. [84].

From the XPS analysis, the amount of sp^3-bonded C and sp^2-C, as the ratio between the integral intensities of each component, could be extracted. The XPS spectra exhibited a very complex shape pointing to the existence of different chemical states for C 1s (Figure 17).

Three components were needed in order to assure a good fit, associated with the sp^3-C (286 eV) and sp^2-C (284.3 eV) contributions, as well as to C–O, C=O, and/or O–C=O bonds (287.5–289.9 eV) owing most probably to the contamination of the sample surface [180–182]. The deconvolution studies of the C 1s spectra generally reveal two main distinct peaks assignable to sp^2- and sp^3-C hybridization [182]. The peak placed at a higher binding energy (BE) is assigned to sp^3-bonded carbon (C–C and C–H), and that at lower BE corresponds to the sp^2 hybridization state of carbon. From the analysis of the main components of C 1s core level spectra, one could assume that the amount of sp^2 bonded C decreases from 36% in D20 sample to about 10% in D100. When the methane dilution is increased (D60 and D100), the sp^3-C concentration strongly increases (to ~78 and 87%, respectively).

The increase in the sp^3 content with the augmentation of the methane concentration has been confirmed both by Raman and XPS. A significant sp^3 content augmentation from sample D20 to D100 was measured. This could be the effect of the initial sp^3 hybridization of carbon in the methane molecule. Bugaev et al. [183] also reported that high-quality DLC films can be obtained from pure methane, their results pointing that most probably methyl mechanism is favoring diamond-like bonds formation. It is known that CH_3 are the most abundant species in pure methane discharges, while carbon dimer C2 is the most abundant in methane highly diluted in argon discharges [184, 185].

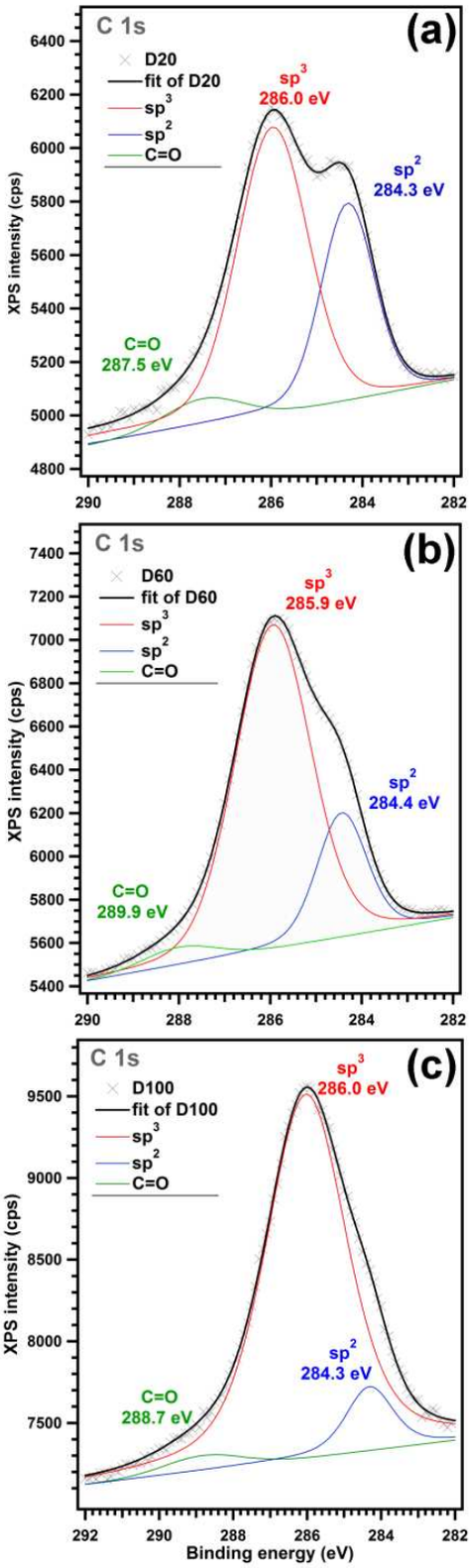

Figure 17. High-resolution XPS spectra for C 1s core level photoelectron after sputter cleaning: samples (a) D20, (b) D60 and (c) D100. Reproduced from Popa et al. [84].

3.4.2. Surface energy

Using deionized water and formamide as standard solvents, solid surface energy calculations based on CA measurements were performed. The measurements of the prepared DLC structures were carried out using the goniometric method, the two solvents being dropped onto the surface and the CA estimated. The drop size and the drip distance were kept constant in all cases. The CA values were determined by the evaluation of the tangent angle of a sessile liquid drop on the DLC solid surface. The surface energy was calculated using the Owens–Wendt approximation [186, 187].

The surface energy values recorded for DLC/Ti structures were lower than those of the bare medical grade Ti and PMMA control substrates (see Table 11).

Sample	Deposition atmosphere composition	Surface energy (mJ/m^2)
Bare Ti	N/A	37.85 ± 0.94
PMMA	N/A	36.35 ± 0.78
D20	20% CH_4 + 80% Ar	32.09 ± 0.73
D60	60% CH_4 + 40% Ar	30.50 ± 0.70
D100	100% Ar	28.71 ± 0.34

Table 11. Surface energy values recorded for the DLC TFs, and for the Ti and PMMA controls. Reproduced from Popa et al. [84].

One notices a decrease of the surface energy with the increase of methane dilution in the reactor chamber (Table 11). The two tailed *t*-testing showed statistically significant differences ($p < 0.05$) between the surface energy values recorded for all samples. An important decrease (with ~25%) of the surface energy was obtained when applying the DLC coating: from 37.85 ± 0.94 mJ/m^2 for the bare Ti substrate down to 28.7 ± 0.34 mJ/m^2 for the D100 structure.

3.4.3. DLC films interaction with blood

Platelets were obtained by centrifugation of whole blood and their adherence to the DLC films surface was investigated by Western blot method. The detailed procedures for platelets isolation and for the Western blot technique are described in Ref. [84].

The obtained signal is proportional to the amount of beta-actin, a structural protein present in all cells and, therefore, to the number of platelets adhered on the sample surface at the moment of lysis. As visible from Figure 18, there was almost the same number of platelets present on the surface of bare titanium and D20 samples.

The number of platelets adhered on D60 and D100 was significantly lower. The DLC coatings ensure conditions for a weaker platelet–surface interaction, which in vivo can conduct to a lower platelet activation and subsequently a prolonged time of coagulation. One can assert that this effect derives from the fact that all cells have a negatively charged cellular membrane,

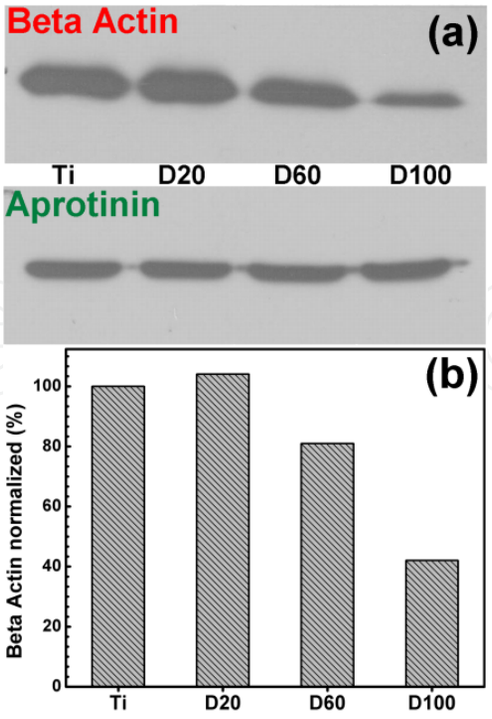

Figure 18. (a) Western blot analysis of beta-actin and aprotinin present in platelets adhered on DLC and bare Ti samples; (b) optical density histograms of normalized quantity of beta-actin present in platelets adhered on DLC and bare Ti samples. Reproduced from Popa et al. [84].

which tends to interact/adhere to positively charged surfaces (hydrophilic surfaces) rather than to hydrophobic ones.

The polyvinylidene fluoride membranes were also probed with aprotinin (a protease inhibitor with proteic structure and a mass of ~6 kDa), which was present in the same concentration in all samples, since it was added to the lysis buffer formulation. This is an internal quality control which ensures that all steps of the technique are properly done.

The results of protein adsorption on the DLC surfaces are shown in Figure 19.

Figure 19a shows that serum albumin was adsorbed in greater quantities on all DLC surfaces than on the bare titanium surface [albumin molecular weight (MW) ~66,483 Da]. Other proteins (G immunoglobulins) presented a roughly similar pattern (G immunoglobulins MW ~134,350 Da). Another important peak is that of 28,900 Da, which can be assigned to the factor XIIa light chain and is more prominent on the titanium sample (Figure 19b). The factor XII, the activator of surface contact coagulation cascade, could not be identified because it had a mass similar to that of albumin (factor XII MW ~67,792 Da).

Albumin is a protein that has hydrophobic moieties, being a blood carrier for many hydrophobic molecules. Since our DLC surfaces tend to be more hydrophobic, it is expected to find more adsorbed albumin than on titanium as confirmed by mass spectroscopy spectra. The vast majority of proteins in blood are glycosylated, which makes them more hydrophilic and more susceptible to polar interactions. The quantity of albumin adsorbed on the surface shields the surface of the sample, making it difficult for the different proteins and coagulation factors to

http://dx.doi.org/10.5772/60808

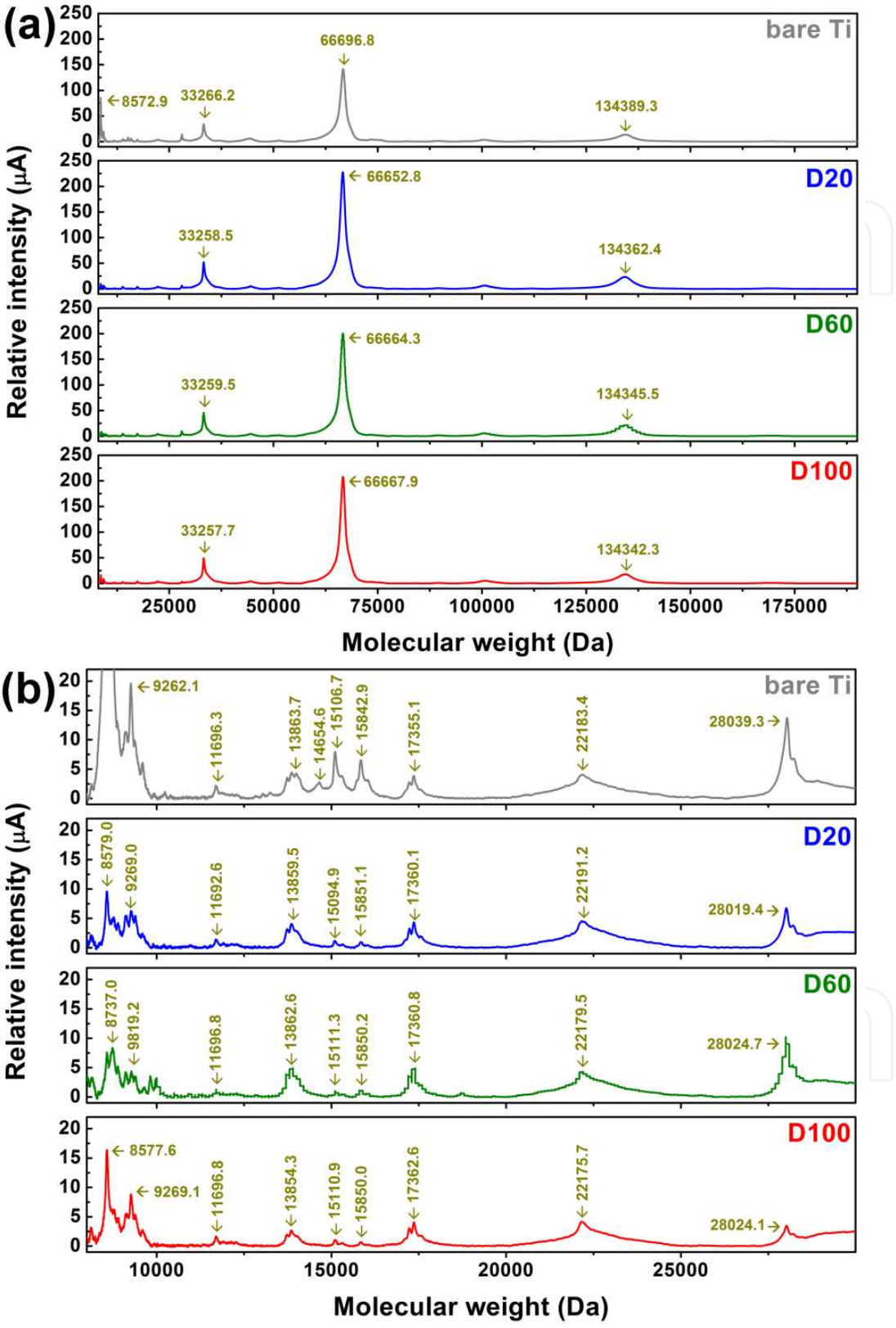

Figure 19. (a) SELDI-ToF complete spectra of proteins adsorbed on DLC and bare Ti samples from fresh blood plasma; (b) SELDI-ToF detailed spectra in MW range 8000–30,000 Da. Reproduced from Popa et al. [84].

reach the sample and activate the coagulation cascade (Figure 19b). These findings are in line with Liu et al. [188], who showed that the albumin adsorption on DLC inactivates the surface for blood clotting. One can state that the coagulation time for each material is in line with surface energy data, with the platelet–surface adherence properties and protein adsorption profiles, and so advocates for a cause–effect relationship between these factors.

4. Conclusions

Wettability of solid substrates represents an important phenomenon for many natural systems and can play a key role in a wide range of applications such as coatings, tunable surfaces, design of hydrophobic/superhydrophobic, or hydrophilic surfaces. It is well known that the wettability of a solid surface is governed by both surface structure and chemistry. After a brief introduction on wettability of nanostructures and the possibility to investigate it by contact angle (CA) measurements, this chapter focused on hydrophobic and hydrophilic structures (oxide and DLC TFs or NPs) synthesized by various deposition techniques (PLD, SG, TE, solution based on chemical approaches, sputtering, and PECVD).

The possibility of tuning the wetting behavior of textile materials by their functionalization with oxide TFs or NPs was reviewed. Depending on the deposition ambience, the TFs can change their behavior from hydrophilic when obtained in an oxygen flux to superhydrophobic when deposited in vacuum. The hydrophobicity was found consistent with the organization of the deposits in vacuum consisting of nanometric crystallites. The subsequent treatment with a TF of a fusion hydrophobin, deposited by soaking in solution, and a ZnO TF finishing in vacuum boosted the antifungal efficiency of the structure by 100%. This significant enhancement was attributed to the higher texturing of the oxide film when growing on hydrophobin interlayer, resulting in an increased presence of oxygen species on surface. In complementary studies, fabrics functionalized with oxide layers showed improved UV protective performances. These results might offer guidance for laser manufacturing in one technological step of stable superhydrophobic and antifungal textile surfaces, used for everyday garments and medical clothing.

ZnO structures can present different degrees of compactness, and as a consequence, they can trap more or less air. This result can be explained by the Cassie–Baxter model. Due to the morphology of the deposited ZnO structure, which is made of a large number of small prisms, the roughness presents high values. The apparent CA is therefore enhanced as compared to the one measured on a similar smooth surface. When the space between the ZnO structures is large enough, the water droplet can penetrate, and an explanation of the phenomenon can be based on the Wenzel model. There exists also the possibility to obtain a transition between these two regimes, and the apparent CA could be different than the one inferred for a smooth surface.

CA measurements confirmed that the presence of SiO_x particles on fiber surfaces can change the wetting behavior of the structure. Since it brings OH groups to the surface, the deposition of SiO_x is therefore expected to provide hydrophilic properties to the textiles.

Although bulk polyester is hydrophobic, water droplets can be sucked into the fibers due to high porosity (void areas) of the material. The void areas were drastically reduced by the addition of TiO_2 particles. They decrease the voids and concomitantly increase the sample hydrophobicity. Under these complex conditions, one cannot use the traditional equations like Cassie–Baxter or Wenzel to model the wettability behavior of the heterogeneous and rough samples.

Protein adsorption using fresh blood plasma from healthy patients was also studied. In the case of DLC films with the highest sp^3 content, albumin was preferentially adsorbed (due to the affinity between the surface and the hydrophobic moieties of the protein), thus shielding the surface and preventing the immobilization of coagulation factors.

The results reviewed in this chapter are devoted to improve the understanding of the wettability of nanostructured surfaces. Understanding the importance of surface wettability and succeeding to control this phenomenon at nanometric scale will hopefully facilitate the fabrication of devices with improved characteristics for top applications, especially in nanotechnology.

Acknowledgements

LD and INM acknowledge project no. 7-083/2014 (CARLA). IZ acknowledges the financial support of the Romanian Ministry of Education and Research under the Project IDEI 281/2011. ACP acknowledges the funding of this research by the Romanian National Authority for scientific research through PNII-RU-TE-2012-3-0379 (TE 16/2013).

Author details

L. Duta[1], A.C. Popescu[1], I. Zgura[2], N. Preda[2] and I.N. Mihailescu[1*]

*Address all correspondence to: ion.mihailescu@inflpr.ro

1 National Institute for Lasers, Plasma, and Radiation Physics, Magurele, Romania

2 National Institute of Materials Physics, Magurele, Romania

References

[1] Duta L., Popescu A.C., Dorcioman G., Mihailescu I.N., Stan G.E., Zgura I., Enculescu I., Dumitrescu I. ZnO thin films deposited on textile material substrates for biomedical applications. In: Vaseashta A., Braman E., Susmann P. (eds.), Technological inno-

vations in sensing and detection of chemical, biological, radiological, nuclear threats and ecological terrorism. Netherlands: Springer; 2012.

[2] Yamamoto O. Influence of particle size on the antibacterial activity of zinc oxide. International Journal of Inorganic Materials. 2001;3(7) 643–646.

[3] Rajendran R., Balakumar C., Mohammed Ahammed H.A., Jayakumar S., Vaideki K., Rajesh E.M. Use of zinc oxide nano particles for production of antimicrobial textiles. International Journal of Engineering, Science and Technology. 2010;2(1) 202–208.

[4] Brayner R., Ferrari-Iliou R., Brivois N., Djediat S., Benedetti M.F., Fievet F. Toxicological impact studies based on *Escherichia coli* bacteria in ultrafine ZnO nanoparticles colloidal medium. Nano Letters. 2006;6(4) 866–870.

[5] Yamamoto O., Komatsu M., Sawai J., Nakagawa Z.E. Effect of lattice constant of zinc oxide on antibacterial characteristics. Journal of Materials Science: Materials in Medicine. 2004;15(8) 847–851.

[6] Huang Z., Zheng X., Yan D., Yin G., Liao X., Kang Y., Yao Y., Huang D., Hao B. Toxicological effect of ZnO nanoparticles based on bacteria. Langmuir 2008;24(8) 4140–4144.

[7] Holysz L., Chibowski E., Terpilowski K. Influence of ambient humidity on the apparent surface free energy of poly(methyl methacrylate) (PMMA). In: Mittal K. (ed.), Contact angle, wettability and adhesion. VSP/Brill: Leiden; 2008. p95–113.

[8] Kubiak K.J., Wilson M.C.T., Mathia T.G., Carval Ph. Wettability versus roughness of engineering surfaces. Wear 2011;271(3–4) 523–528.

[9] Xinjian F, Lei J. Design and creation of superwetting/antiwetting surfaces. Advanced Materials 2006;18(23) 3063–3078.

[10] Whyman G., Bormashenko E., Stein T. The rigorous derivation of Young, Cassie–Baxter and Wenzel equations and the analysis of the contact angle hysteresis phenomenon. Chemical Physics Letters. 2008;450(4–6) 355–359.

[11] Bico J., Tordeux C., Quéré D. Wetting of textured surfaces. Colloid and Surfaces A: Physicochemical and Engineering Aspects. 2002;206(1–3) 41–46.

[12] Rosales-Leal J.I., Rodríguez-Valverde M.A., Mazzaglia G., Ramón-Torregrosa P.J., Díaz-Rodríguez L., García-Martínez O., Vallecillo-Capilla M., Ruiz C., Cabrerizo-Vílchez M.A. Effect of roughness, wettbility and morphology of engineered titanium surfaces on osteoblast-like cell adhesion. Colloids and Surfaces A: Physicochemical and Engineering aspects 2010;365(1–3) 222–229.

[13] Tuteja A., Choi W., Ma M., Mabry J.M., Mazzella S.A., Rutledge G.C., McKinley G.H., Cohen R.H.. Designing superoleophobic surfaces. Science 2007;318(5856) 1618–1622.

[14] Marmur A. Solid-surface characterization by wetting. Annual Review of Materials Research 2009;39 473–489.

[15] Cassie A.B.D., Baxter S. Transactions of the Faraday Society 1944;40() 546–551.

[16] Lafuma A., Quéré D. Superhydrophobic states. Nature Materials 2003;2(7) 457–460.

[17] Ishino C., Okumura K., Quéré D. Wetting transitions on rough surfaces. Europhysics Letters 2004;68(3) 419–425.

[18] Marmur A. The lotus effect: superhydrophobicity and metastability. Langmuir 2004;20(9) 3517–3519.

[19] Dupuis A., Yeomans J.M. Modeling droplets on superhydrophobic surfaces: equilibrium states and transitions. Langmuir 2005;21(6) 2624–2629.

[20] Patankar N.A. On the modeling of hydrophobic contact angles on rough surfaces. Langmuir 2003;19(4) 1249–1253.

[21] Sameer R.P., Zheng C., Wei H., Narendra B.D. Wetting effects on in vitro bioactivity and in vitro biocompatibility of laser micro-textured Ca-P coating. Biofabrication 2010;2(2) 025001.

[22] Adamson A.W., editor. Physical Chemistry of Surfaces. New York: Wiley; 1990.

[23] Tammar S., Meiron A., Sam Saguy I. Contact angle measurement on rough surfaces. Journal of Colloid and Interface Science 2004;274(2) 637–644.

[24] Deepak P.S., Dinesh K.M., Ashish S., Ujjwal M.J., Andrzej H. Study of the wettability of ZnO nanofilms. International Nano Letters 2011;1(2) 117–122.

[25] Yin-Yu C., Chih-Ho L., Jui-Ting H., Chih-Hsin T., Wan-Chuen L., Heng-Li H. Antibacterial properties and human gingival fibroblast cell compatibility of TiO_2/Ag compound coatings and ZnO films on titanium-based material. Clinical Oral Investigations 2012;16(1) 95–100.

[26] Helena T., Patrycja S-WoŸ, Marta F., Iwona K. Deposition of Zinc Oxide on the materials used in medicine. Preliminary results. Fibres and Textiles in Eastern Europe 2014;3(105) 126–132.

[27] Kaushalkumar B., Duncan R., Radhakrishna P., Pat P. LED-controlled tuning of ZnO nanowires' wettability for biosensing applications. Nano Reviews 2015;6() 26711.

[28] Mao-Gang G., Xiao-Liang X., Zhou Y., Yan-Song L., Ling L. Superhydrophobic surfaces via controlling the morphology of ZnO micro/nano complex structure. Chinese Physics B 2010;19(5) 056701.

[29] Amirhosein B., Ramin K., Mohammad E.Y. Fabrication of superhydrophobic and antibacterial surface on cotton fabric by doped silica-based sols with nanoparticles of copper. Nanoscale Research Letters 2011;15,6(1) 594.

[30] Yang S., Guixue W., Xianliang H., Qin Z., Jiang W., Chaojun T., Qingsong Y., Xiaoheng L. Surface wettability of plasma SiO_x:H nanocoating-induced endothelial

cells'migration and the associated FAKRho GTPases signalling pathways. Journal of the Royal Society Interface 2012;9(67) 313–327.

[31] Antonia T., Jose IV-P., de la Orden E., Yubero F., Gonzalez-Caballero J.L., González-Elipe A.R., Vilches J., Salido M. Osteoconductive potential of barrier nanoSiO_2 PLGA membranes functionalized by plasma enhanced chemical vapour deposition. Bio-Medical Research International 2014;2014() 253590.

[32] Brown P.S., Bhushan B. Mechanically durable, superoleophobic coatings prepared by layer-by-layer technique for anti-smudge and oil-water separation. Scientific Reports 2014;5() 8701.

[33] Anitha V.C., Lee J.H., Lee J., Banerjee A.N., Joo S.W., Min B.K. Biofilm formation on a TiO_2 nanotube with controlled pore diameter and surface wettability. Nanotechnology 2015;26(6) 065102.

[34] Hyde G.K., Stewart S.M., Scarel G., Parsons G.N., Shih C.C., Shih C.M., Shing-Jong L., Yea-Yang S., Monteiro-Riviere N.A., Narayan R.J. Atomic layer deposition of titanium dioxide on cellulose acetate for enhanced hemostasis. Biotechnology Journal 2011;6(2) 213–223.

[35] Terumitsu H., So N., Aki K., Myoung-Woon M., Yousuke K., Atsushi H., Kwang-Ryeol L., Koki T., Takuji Y., Tetsuya S. Hydrophobicity and non-thrombogenicity of nanoscale dual rough surface coated with fluorine-incorporated diamond-like carbon films: biomimetic surface for blood-contacting medical devices. Diamond and Related Materials 2013;38 14–18.

[36] Terumitsu H., Atsushi S., Tetsuya S., Yoshiaki M., Toshiya S., Satoshi Y., Aki K., Nobuyuki S., Mutsumi H., Kanako K., Hirokuni Y., Sachio K. Fluorinated diamond-like carbon as antithrombogenic coating for blood-contacting devices. Journal of Biomedical Materials Research Part A 2006;76A(1), 86–94.

[37] Salgueiredo E., Vila M., Silva M.A., Lopes M.A., Santos J.D., Costa F.M., Silva R.F., Gomes P.S., Fernandes M.H. Biocompatibility evaluation of DLC-coated Si3N4 substrates for biomedical applications. Diamond and Related Materials 2008;17(4–5) 878–881.

[38] Shanhong W., Liping W., Qunji X. Super-hydrophilic properties of TiO_2–DLC nanocomposite films fabricated by the simple electrochemical process. Applied Surface Science 2011;257(23) 10000–10004.

[39] Leonard R.L., Terekhov A.Y., Thompson C., Erck R.A., Johnson J.A. Antifog coating for bronchoscope lens. Surface Engineering 2012;28(6) 468–472.

[40] Jones D.S., Garvin C.P., Dowling D., Donnelly K., Gorman S.P. Examination of surface properties and in vitro biological performance of amorphous diamond-like carbon-coated polyurethane. Journal of Biomedical Materials Research Part B: Applied Biomaterials 2006;78(2) 230–236.

[41] Gao I., McCarthy T.J. Contact angle hysteresis explained. Langmuir 2006;22(14) 6234–6237.

[42] www.attension.com (last accessed 14 April 2015).

[43] Miwa M., Nakajima A., Fujishima A., Hashimoto K., Watanabe T. Effects of the surface roughness on sliding angles of water droplets on superhydrophobic surfaces. Langmuir 2000;16(13) 5754–5760.

[44] McHale G., Shirtcliffe N.J., Newton M.I. Contact angle hysteresis on super-hydrophobic surfaces. Langmuir 2004;20(23) 10146–10149.

[45] Furmidge C.G.L. Studies at phase interfaces. I. The sliding of liquid drops on solid surfaces and a theory for spray retention. Journal of Colloid and Interface Science 1962;17(4) 309–324.

[46] Feng L., Li S., Li Y., Li H., Zhang L., Zhai J., Song Y., Liu B., Jiang L., Zhu D. Superhydrophobic surfaces: from natural to artificial. Advanced Materials 2002;14(24) 1857–1860.

[47] Blossey R. Self-cleaning surfaces - virtual realities. Nature Materials 2003;2 301–306.

[48] Zisman W.A. Relation of the equilibrium contact angle to liquid and solid constitution. In: Fowkes F.M. (ed.), Advances in Chemistry. American Chemical Society. 1964; p1–51.

[49] Fox H.W., Zisman A.W. The spreading of liquids on low-energy surfaces. II. Modified tetrafluoroethylene polymers. Journal of Colloid and Interface Science 1952;7(2) 109–121.

[50] Hejda F., Solar P., Kousal J. Surface free energy determination by contact angle measurements—a comparison of various approaches. In: Safrankova J, Pavlu J. (eds.), WDS'10 Proceedings of Contributed Papers: Part III—Physics, 1–4 June 2010, Prague. Matfyzpress.

[51] Sharma P.K., Rao K.H. Analysis of different approaches for evaluation of surface energy of microbial cells by contact angle goniometry. Advances in Colloid and Interface Science 2002;98(3) 341–463.

[52] Patra S., Sarkar S., Bera S.K., Ghosh R., Paul G.K. Hydrophobic self-cleaning surfaces of ZnO thin films synthesized by sol-gel technique. Journal of Physics D: Applied Physics. 2009;42(7) 075301.

[53] Zhang Z., Chen H., Zhong J., Saraf G., Lu Y. Fast and reversible wettability transitions on ZnO nanostructures. Journal of Electronic Materials. 2007;36(8) 895–899.

[54] Irzh A., Genish I., Klein L., Solovyov L.A., Gedanken A. Synthesis of ZnO and Zn nanoparticles in microwave plasma and their deposition on glass slides. Langmuir 2010;26(8) 5976–5984.

[55] Han J., Gao W. Surface wettability of nanostructured zinc oxide films. Journal of Electronic Materials. 2009;38(4) 601–608.

[56] Patra S., Sarkar S., Bera S.K., Paul G.K., Ghosh R. Influence of surface topography and chemical structure on wettability of electrodeposited ZnO thin films. Journal of Applied Physics. 2010;108(8) 083507.

[57] Kekkonen V., Hakola A., Kajava T., Sahramo E., Malm J., Karppinen M., Ras R.H.A. Self-erasing and rewritable wettability patterns on ZnO thin films. Applied Physics Letters. 2010;97(4) 044102.

[58] He S., Zheng M., Yao L., Yuan X., Li M., Ma L., Shen W. Preparation and properties of ZnO nanostructures by electrochemical anodization method. Applied Surface Science. 2010;256(8) 2557–2562.

[59] Eason R., editor. Pulsed laser deposition of thin films: applications-lead growth of functional materials. Wiley-Blackwell; 2007.

[60] Singh A., Davis E.A. The a-SiO*x*:H*y* thin film system I. Structural study by IR spectroscopy. Journal of Non-Crystalline Solids 1990;122(3) 223–232.

[61] Leplan H., Robic J.Y., Pauleau Y. Kinetics of residual stress evolution in evaporated silicon dioxide films exposed to room air. Journal of Applied Physics. 1996;79(9) 6926–6932.

[62] da Silva Sobrinho A.S., Czeremuszkin G., Latreche M., Wertheimer M.R. Defect-permeation correlation for ultrathin transparent barrier coatings on polymers. Journal of Vacuum Science and Technology A. 2000;18(1) 149–158.

[63] Madocks J., Rewhinkle J., Barton L. Packaging barrier films deposited on PET by PECVD using a new high density plasma source. Materials Science and Engineering: B. 2005;119(3) 268–273.

[64] Leterrier Y. Durability of nanosized oxygen-barrier coatings on polymers. Progress in Materials Science. 2003;48(1) 1–55.

[65] Anastasescu C., Anastasescu M., Teodorescu V.S., Gartner M., Zaharescu M. SiO_2 nanospheres and tubes obtained by sol-gel method. Journal of Non-Crystalline Solids. 2010;356(44–49) 2634–2640.

[66] Bae G.Y., Min B.G., Jeong Y.G., Lee S.C., Jang J.H., Koo G.H. Superhydrophobicity of cotton fabrics treated with silica nanoparticles and water-repellent agent. Journal of Colloid and Interface Science 2009;337(1) 170–175.

[67] Yang C., Fan H., Xi Y., Chen J., Li Z. Effects of depositing temperatures on structure and optical properties of TiO_2 film deposited by ion beam assisted electron beam evaporation. Applied Surface Science. 2008;254(9) 2685–2689.

[68] da Silva Sobrinho A.S., Czeremuszkin G., Latreche M., Wertheimer M.R. Defect-permeation correlation for ultrathin transparent barrier coatings on polymers. Journal of

Vacuum Science and Technology. A, Vacuum, Surfaces, and Films. 2000;18(1) 149–157.

[69] Sonnenfeld A., von Rohr P.R., Hauert R. UV Absorptance of titanium dioxide thin films by plasma enhanced deposition from mixtures of oxygen and titanium-tetrakis-isopropoxide. Plasma Chemistry and Plasma Processing. 2006;26(3) 319–334.

[70] Carneiro J.O., Teixeira V., Nascimento J.H.O., Neves J., Tavares P.B. Photocatalytic activity and UV-protection of TiO_2 nanocoatings on poly(lactic acid) fibres deposited by pulsed magnetron sputtering. Journal of Nanoscience and Nanotechnology 2011;11(10) 8979–8985.

[71] Xu Y., Xu W., Huang F., Wei Q.F. Preparation and photocatalytic activity of TiO_2-deposited fabrics. International Journal of Photoenergy. 2012;852675.

[72] Ojstrsek A., Kleinschek K.S., Fakin D. Characterization of nano-sized TiO_2 suspensions for functional modification of polyester fabric. Surface and Coatings Technology. 2013;226 68–74.

[73] Pisitsak P., Samootsoot A., Chokpanich N. Investigation of the self-cleaning properties of cotton fabrics finished with nano-TiO_2 and nano-TiO_2 mixed with fumed silica. KKU Research Journal. 2013;18(2) 200–211.

[74] Watanabe Y., Kobayashi T., Kirihara S., Miyamoto Y., Sakoda K. Cotton-yarn/TiO_2 dispersed resin photonic crystals with straight and wavy structures. European Physical Journal B. 2004;39(3) 295–300.

[75] Asadi M., Montazer M. Multi-functional polyester hollow fiber nonwoven fabric with using nano clay/nano TiO_2/polysiloxane composites. Journal of Inorganic and Organometallic Polymers and Materials. 2013;23(6) 1358–1367.

[76] Macwan D., Dave P.N., Chaturvedi S. A review on nano-TiO_2 sol-gel type syntheses and its applications. Journal of Materials Science. 2011;46(11) 3669–3686.

[77] Ning L., Hongyi L., Hong W., Tao C., Jinshu W., Lei C. Studies on the TiO_2 modified microchannels for microfluidic applications. Materials Letters. 2012;89 247–250.

[78] Fusi M., Maccallini E., Caruso T., Casari C.S., Li Bassi A., Bottani C.E., Rudolf P., Prince K.C., Agostino R.G. Surface electronic and structural properties of nanostructured titanium oxide grown by pulsed laser deposition. Surface Science. 2011;605(3–4) 333–340.

[79] Petersen M., Bandorf R., Brauer G., Klages C.P. Diamond-like carbon films as piezoresistors in highly sensitive force sensors. Diamond and Related Materials. 2012;26 50–54.

[80] Oliveira E.C., Cruz S.A., Aguiar P.H.L. Effect of PECVD deposition parameters on the DLC/PLC composition of a-C:H thin films. Journal of the Brazilian Chemical Society. 2012;23(9) 1657–1662.

[81] Vaghri E., Khalaj Z., Ghoranneviss M., Borghei M. Characterization of diamond-like carbon films synthesized by DC-plasma enhanced chemical vapor deposition. Journal of Fusion Energy. 2011;30(5) 447–452.

[82] Logothetidis S. Haemocompatibility of carbon based thin films. Diamond and Related Materials. 2007;16(10) 1847–1857.

[83] Flege S., Hatada R., Ensinger W., Baba K. Properties of hydrogenated DLC films as prepared by a combined method of plasma source ion implantation and unbalanced magnetron sputtering. Journal of Materials Research. 2012;27(5) 845–849.

[84] Popa A.C., Stan G.E., Husanu M.A., Pasuk I., Popescu I.D., Popescu A.C., Mihailescu I.N. Multi-layer haemocompatible diamond-like carbon coatings obtained by combined radio frequency plasma enhanced chemical vapor deposition and magnetron sputtering. Journal of Materials Science: Materials in Medicine. 2013;24(12) 2695–2707.

[85] Myllymaa S., Kaivosoja E., Myllymaa K., Sillat T., Korhonen H., Lappalainen R., Konttinen Y.T. Adhesion, spreading and osteogenic differentiation of mesenchymal stem cells cultured on micropatterned amorphous diamond, titanium, tantalum and chromium coatings on silicon. Journal of Materials Science: Materials in Medicine. 2010;21(1) 329–341.

[86] Soininen A., Levon J., Katsikogianni M., Myllymaa K., Lappalainen R., Konttinen Y.T., Kinnari T.J., Tiainen V.M., Missirlis Y. In vitro adhesion of staphylococci to diamond-like carbon polymer hybrids under dynamic flow conditions. Journal of Materials Science: Materials in Medicine. 2011;22(3) 629–636.

[87] Srinivasan S., Tang Y., Li Y.S., Yang Q., Hirose A. Ion beam deposition of DLC and nitrogen doped DLC thin films for enhanced haemocompatibility on PTFE. Applied Surface Science. 2012;258(20) 8094–8099.

[88] Jelinek M., Smetana K., Kocourek T., Dvorankovac B., Zemek J., Remsa J., Luxbacher T. Biocompatibility and sp3/sp2 ratio of laser created DLC films. Materials Science and Engineering: B. 2010;169(1–3) 89–93.

[89] Pısarık P., Jelınek M., Smetana K. Jr., Dvorankova B., Kocourek T., Zemek J., Chvostova D. Study of optical properties and biocompatibility of DLC films characterized by sp3 bonds. Applied Physics A. 2013;112(1) 143–148.

[90] Nelea V., Jelinek M., Mihailescu I.N. Biomaterials: new issues and breakthroughs for biomedical applications. In: Eason R. (ed.), Pulsed Laser Deposition of Thin Films: Applications-Lead Growth of Functional Materials. Wiley & Sons; 2007. p421–p459.

[91] Boyd I.W. Thin film growth by pulsed laser deposition. Ceramics International 1996;22() 429–434.

[92] Bao Q., Chen C., Wang D., Ji Q., Lei T. Pulsed laser deposition and its current research status in preparing hydroxyapatite thin films. Applied Surface Science 2005;252(5) 1538–1544.

[93] Mihailescu I.N., Gyorgy E. Pulsed laser deposition: an overview. In: Asakura T. (ed.), International Trends in Optics and Photonics. Heidelberg: Springer; 1999. p201–214.

[94] Liste S., Gonzalez P., Serra J., Borrajo J.P., Chiussi S., Leon B., Perez Amor M., Garcıa Lopez J., Ferrer F.J., Morilla Y., Respaldiza M.A. Study of the stoichiometry transfer in pulsed laser deposition of bioactive silica based glasses. Thin Solid Films 2004;453–454 219–223.

[95] Baviskar P.K., Nikam P.R., Gargote S.S., Ennaoui A., Sankapal B.R. Controlled synthesis of ZnO nanostructures with assorted morphologies via simple solution chemistry. Journal of Alloys and Compounds. 2013;551 233–242.

[96] Xu S., Wang Z.L. One-dimensional ZnO nanostructures: solution growth and functional properties. Nano Research. 2011;4(11) 1013–1098.

[97] Pauporte T. Design of solution-grown ZnO nanostructures. In: Wang Z.M. (ed.), Toward Functional Nanomaterials, Lecture Notes in Nanoscale Science and Technology. LLC: Springer Science+Business Media; 2009. p77–125.

[98] Nelea V., Morosanu C., Iliescu M., Mihailescu I.N. Hydroxyapatite thin films grown by pulsed laser deposition and radio-frequency magnetron sputtering: comparative study. Applied Surface Science 2004;228(1–4) 346–356.

[99] Nelea V., Morosanu C., Iliescu M., Mihailescu I.N. Microstructure and mechanical properties of hydroxyapatite thin films grown by RF magnetron sputtering. Surface and Coatings Technology. 2003;173(2–3) 315–322.

[100] Stan G.E. Adherent functional graded hydroxylapatite coatings produced by sputtering deposition techniques. Journal of Optoelectronics and Advanced Materials. 2009;11(8) 1132–1138.

[101] Schneider J.M., Rohde S., Sproul W.D., Matthews A. Recent developments in plasma assisted physical vapour deposition. Journal of Physics D: Applied Physics 2000;33(18) R173.

[102] Berg S., Nyberg T. Fundamental understanding and modeling of reactive sputtering processes. Thin Solid Films. 2005;476(2) 215–230.

[103] Zgura I., Frunza S., Frunza L., Enculescu M., Florica C., Cotorobai V.F., Ganea C.P. Polyester fabrics covered with amorphous titanium dioxide layers: combining wettability measurements and photoinduced hydrophilicity to assess their surface properties. Romanian Reports in Physics. 2016;68(1).

[104] Miller J.D., Veeramasuneni S., Drelich J., Yalamanchili M.R., Yamauchi G. Effect of roughness as determined by atomic force microscopy on the wetting properties of PTFE thin films. Polymer Engineering and Science. 1996;36(14) 1849–1855.

[105] Bahners T.J. The do's and don'ts of wettability characterization in textiles. Journal of Adhesion Science and Technology. 2011;25(16) 2005–2021.

[106] Oldani C., Dominguez A. Titanium as a biomaterial for implants. In: Fokter S. (ed.). Recent Advances in Arthroplasty. Rijeka: InTech; 2012. p149–p162.

[107] Reddy K.M., Feris K., Bell J., Wingett D.G., Hanley C., Punnoose A. Selective toxicity of zinc oxide nanoparticles to prokaryotic and eukaryotic systems. Applied Physics Letters. 2007;90(21) 2139021- 2139023.

[108] Jones N., Ray B., Ranjit K.T., Manna A.C. Antibacterial activity of ZnO nanoparticle suspensions on a broad spectrum of microorganisms. FEMS Microbiology Letters. 2008;279(1) 71–76.

[109] Nair M.G., Nirmala M., Rekha K., Anukaliani A. Structural, optical, photo catalytic and antibacterial activity of ZnO and Co doped ZnO nanoparticles. Materials Letters. 2011;65(12) 1797–1800.

[110] Sawai J., Shoji S., Igarashi H., Hashimoto A., Kokugan T., Shimizu M., Kojima H. Hydrogen peroxide as an antibacterial factor in zinc oxide powder slurry. Journal of Fermentation and Bioengineering. 1998;86(5) 521–522.

[111] Premanathan M., Karthikeyan K., Jeyasubramanian K., Manivannan G. Selective toxicity of ZnO nanoparticles toward Gram-positive bacteria and cancer cells by apoptosis through lipid peroxidation. Nanomedicine: Nanotechnology, Biology, and Medicine. 2011;7(2) 184–192.

[112] Applerot G., Lipovsky A., Dror R., Perkas N., Nitzan Y., Lubart R., Gedanken A. Enhanced antibacterial activity of nanocrystalline ZnO due to increased ROS-mediated cell injury. Advanced Functional Matterials. 2009;19(6) 842–852.

[113] Carminna O., Andrea L., Marco F., Valentina C. Wetting behavior of hierarchical oxide nanostructures: TiO_2 nanotubes from anodic oxidation decorated with ZnO nanostructures. Journal of the Electrochemical Society. 2014;161(10) D484-D488.

[114] Djuriisic A.B., Ng A.M.C., Chen X.Y. ZnO nanostructures for optoelectronics: material properties and device applications. Progress in Quantum Electronics. 2010;34(4) 191–259.

[115] Ozgur U., Alivov Ya.I., Liu C., Teke A., Reshchikov M.A., Dogan S., Avrutin V., Cho S.-J., Morkoc H. A comprehensive review of ZnO materials and devices. Journal of Applied Physics. 2005;98(4) 041301.

[116] Sontakke T.K., Jagtap R.N., Singh A., Kothari D.C. Nano ZnO grafted on MAA/BA/MMA copolymer: an additive for hygienic coating. Progress in Organic Coatings 2012;74(3) 582–588.

[117] Hochmannova L., Vytrasova. Photocatalytic and antimicrobial effects of interior paints. Progress in Organic Coatings. 2010;67(1) 1–5.

[118] Arya S.K., Saba S., Ramirez-Vick J.E., Gupta V., Bhansali S., Singh S.P. Recent advances in ZnO nanostructures and thin films for biosensor applications: review. Analytica Chimica Acta. 2012;737 1–21.

[119] Loh L., Dunn S. Recent progress in ZnO-based nanostructured ceramics in solar cell applications. Journal of Nanoscience and Nanotechnology 2012;12(11) 8215–8230.

[120] Zhang Y., Yan X., Yang Y., Huang Y., Liao Q., Qi J. Scanning probe study on the piezotronic effect in ZnO nanomaterials and nanodevices. Advanced Materials. 2012;24(34) 4647–4655.

[121] Singh D.P. Synthesis and growth of ZnO nanowires. Science of Advanced Materials. 2010;2 245–272.

[122] Wang Z.L. ZnO nanowire and nanobelt platform for nanotechnology. Materials Science and Engineering: R 2009;64(3–4) 33–71.

[123] Baruah S., Dutta J. Hydrothermal growth of ZnO nanostructures. Science and Technology of Advanced Materials. 2009;10(1) 013001.

[124] Wood T.J., Hurst G.A., Schofield W.C.E., Thompson R.L., Oswald G., Evans J.S.O., Sharples G.J., Pearson C., Petty M.C., Badyal J.P.S. Electroless deposition of multifunctional zinc oxide surfaces displaying photoconductive, superhydrophobic, photowetting, and antibacterial properties. Journal of Materials Chemistry. 2012;22(9) 3859–3867.

[125] Lee M., Kwak G., Yong K. Wettability control of ZnO nanoparticles for universal applications. ACS Applied Materials and Interfaces. 2011;3(9) 3350–3356.

[126] Lee S. Developing UV-protective textiles based on electrospun zinc oxide nanocomposite fibers. Fibers and Polymers. 2009;10(3) 295–301.

[127] Zhang J., Huang W., Han Y. Wettability of zinc oxide surfaces with controllable structures. Langmuir 2006;22(7) 2946–2950.

[128] Maheswari R., editor. Fungi: Experimental Methods in Biology. Boca Raton: CRC press; 2011.

[129] Kisko K., Szilvay G.R., Vuorimaa E., Lemmetyinen H., Linder M.B., Torkkeli M., Serimaa R. Self-assembled films of hydrophobin proteins HFBI and HFBII studied in situ at the air/water interface. Langmuir 2009;25(3) 1612–1619.

[130] Cox P.W., Hooley P. Hydrophobins: new prospects for biotechnology. Fungal Biology Reviews. 2009;23(1–2) 40–47.

[131] Liu J., Liu C., Liu Y., Chen M., Hu Y., Yang Z. Study on the grafting of chitosan–gelatin microcapsules onto cotton fabrics and its antibacterial effect. Colloids and Surfaces B: Biointerfaces. 2013;109 103–108.

[132] Perelshtein I., Ruderman E., Perkas N., Tzanov T., Beddow J., Joyce E., Mason T.J., Blanes M., Molla K., Patlolla A., Frenkele A.I., Gedanken A. Chitosan and chitosan-ZnO-based complex nanoparticles: formation, characterization, and antibacterial activity. Journal of Materials Chemistry B 2013;1(14) 1968–1976.

[133] Zemljic L.F., Sauperl O., Kreze T., Strnad S. Characterization of regenerated cellulose fibers antimicrobial functionalized by chitosan. Textile Research Journal 2013;83(2) 185–196.

[134] Nithyakalyani D., Ramachandran T., Rajendran R., Mahalakshmi M. Assessment of antibacterial activity of herbal finished surface modified polypropylene nonwoven fabric against bacterial pathogens of wound. Journal of Applied Polymer Science. 2013; 129(2) 672–681.

[135] Kerkeni A., Behary N., Dhulster P., Chihib N.E., Perwuelz A. Study on the effect of plasma treatment of woven polyester fabrics with respect to nisin adsorption and antibacterial activity. Journal of Applied Polymer Science. 2013;129(2) 866–873.

[136] Gao Y., Yu X., Pierlot A.P., Denning R.J., Cranston R. A simultaneous antimicrobial and shrink resistance treatment of wool woven fabrics using the polymeric biocide polyhexamethylene biguanide. Journal of Materials Science. 2011;46(9) 3020–3026.

[137] Gowri V.S., Almeida L., de Amorim M.T.P., Pacheco N.C., Souto A.P., Esteves M.F., Sanghi S.K. Functional finishing of polyamide fabrics using ZnO-PMMA nanocomposites. Journal of Materials Science. 2010;45(9) 2427–2435.

[138] Subkowski T., Karos M., Subkowski T. Industrial performance proteins: hydrophobin-learning from nature. Journal of Biotechnology. 2007;131(2) S212-S213.

[139] Yang J., Zhang Z., Men X., Xu X., Zhu X. Reversible superhydrophobicity to superhydrophilicity switching of a carbon nanotube film via alternation of UV irradiation and dark storage. Langmuir. 2010;26(12) 10198–10202.

[140] Papadopoulou E.L., Zorba V., Pagkozidis A., Barberoglou M., Stratakis E., Fotakis C. Reversible wettability of ZnO nanostructured thin films prepared by pulsed laser deposition. Thin Solid Films. 2009;518(4) 1267–1270.

[141] Popescu AC, Dorcioman G, Duta L, Mihailescu IN, Stan GE, Pasuk I, Zgura I, Beica T, Enculescu I, Ianculescu A, Dumitrescu I. Radical modification of the wetting behavior of textiles coated with ZnO thin films and nanoparticles when changing the ambient pressure in the pulsed laser deposition process. Journal of Applied Physics 2011;110(6) 064321.

[142] Bhushan B., Jung Y.C. Natural and biomimetic artificial surfaces for superhydrophobicity, self-cleaning, low adhesion, and drag reduction. Progress in Materials Science. 2011;56(1) 1–108.

[143] Popescu A.C., Stan G.E., Duta L., Dorcioman G., Iordache O., Dumitrescu I., Pasuk I., Mihailescu I.N. Influence of a hydrophobin underlayer on the structuring and antimicrobial properties of ZnO films. Journal of Materials Science. 2013;48(23) 8329–8336.

[144] Schaaf P. (ed.), Laser Processing of Materials. Berlin: Springer; 2011.

[145] Janssen M.I., van Leeuwen M.B.M., Scholtmeijer K., van Kooten T.G., Dijkhuizen L., Wosten H.A.B. Coating with genetic engineered hydrophobin promotes growth of fibroblasts on a hydrophobic solid. Biomaterials. 2002;23(24) 4847–4854.

[146] Boeuf S., Throm T., Gutt B., Strunk T., Hoffmann M., Seebach E., Muhlberg L., Brocher J., Gotterbarm T., Wenzel W., Fischer R., Richter W. Engineering hydrophobin DewA to generate surfaces that enhance adhesion of human but not bacterial cells. Acta Biomaterialia. 2012;8(3) 1037–1047.

[147] Preda N, Enculescu M, Zgura I, Socol M, Matei E, Vasilache V, Enculescu I. Superhydrophobic properties of cotton fabrics functionalized with ZnO by electroless deposition. Materials Chemistry and Physics 2013;138(1) 253–261.

[148] Carp O., Huisman C.L., Reller A. Photoinduced reactivity of titanium dioxide. Progress in Solid State Chemistry. 2004;32(1–2) 33–177.

[149] Hashimoto K., Irie H., Fujishima A. TiO_2 photocatalysis: a historical overview and future prospects. Japanese Journal of Applied Physics. 2005;44(12) 8269–8285.

[150] I. Zgura, S. Frunza, M. Enculescu, C. Florica, F. Cotorobai. Deposition of titanium dioxide layers upon polyester textile materials: checking the adherence by ultra-sonication. Romanian Journal of Physics. Accepted June 2015.

[151] Voinea M., Vladuta C., Bogatu C., Duta A. Surface properties of copper based cermet materials. Materials Science and Engineering: B. 2008;152(1–3) 76–80.

[152] Zgura I, Beica T, Mitrofan IL, Mateias CG, Parvu D, Patrascu I. Assessment of the impression materials by investigation of the hydrophilicity. Digest Journal of Nanomaterials and Biostructures 2010;5(3) 749–755.

[153] Ashraf M., Campagne C., Perwuelz A., Champagne P., Leriche A., Courtois C. Development of superhydrophilic and superhydrophobic polyester fabric by growing zinc oxide nanorods. Journal of Colloid and Interface Science. 2013;394 545–553.

[154] Erbil H.Y., Cansoy C.E. Range of applicability of the Wenzel and Cassie−Baxter equations for superhydrophobic surfaces. Langmuir. 2009;25(24) 14135–14145.

[155] Myint M.T.Z., Kitsomboonloha R., Baruah S., Dutta J. Superhydrophobic surfaces using selected zinc oxide microrod growth on ink-jetted patterns. Journal of Colloid and Interface Science. 2011;354(2) 810–815.

[156] Howells D.G., Henry B.M., Madocks J., Assender H.E. High quality plasma enhanced chemical vapour deposited silicon oxide gas barrier coatings on polyester films. Thin Solid Films. 2008;516(10) 3081–3088.

[157] Textor T., Mahltig B. A sol-gel based surface treatment for preparation of water repellent antistatic textiles. Applied Surface Science. 2010;256(6) 1668–1674.

[158] Alongi J., Tata J., Frache A. Hydrotalcite and nanometric silica as finishing additives to enhance the thermal stability and flame retardancy of cotton. Cellulose 2011;18(1) 179–190.

[159] Beica T., Frunza S., Zgura I., Frunza L., Cotarlan C., Negrila C., Vlaicu A.M., Zaharia C.N. Nanostructured gold layers. I. Deposition by Vacuum evaporation at small angles of incidence. Journal of Optoelectronics and Advanced Materials. 2010;12(2) 347–353.

[160] Zgura I., Beica T., Frunza S., Rasoga O., Galca A., Frunza L., Moldovan A., Dinescu M., Zaharia C. Nanostructured gold layers. II. Gold deposition onto polystyrene substrate. Journal of Optoelectronics and Advanced Materials. 2010;12(2) 354–359.

[161] Zgura I., Beica T., Frunza S., Frunza L., Cotirlan-Simioniuc C., Ungureanu F., Gheorghe N., Rasoga O., Velula T., Zaharia C. Nanostructured gold layers. III. Functionalization of gold layers obliquely deposited onto polystyrene substrate. Journal of Optoelectronics and Advanced Materials. 2010;12(8) 1729–1738.

[162] Zgura I., Beica T., Frunza S., Frunza L., Ganea P., Ungureanu F., Negrila C., Nuta A., Sorescu A.-A., Bunea I., Zaharia C.N. Nanostructured SiOx layers as substrates for liquid crystal local ordering. I. Functionalization to bind bovine serum albumin. Optoelectronics and Advanced Materials—Rapid Communications. 2011;5(3) 318–323.

[163] Frunza L., Zgura I., Enculescu M., Frunza S., Ganea C.P., Rasoga O., Cotorobai F., Dorogan A. Polyester fabrics coated with SiOx nanoparticles by vacuum deposition at small angle. Structural characterization and wetting properties. Journal of Optoelectronics and Advanced Materials. 2014;16(1–2) 176–181.

[164] Dai D., Fan M. Characteristic and performance of elementary hemp fibre. Materials Sciences and Applications. 2010;1(6) 336–342.

[165] Zgura I., Moldovan R., Negrila C.C., Frunza S., Cotorobai V.F., Frunza L. Surface free energy of smooth and dehydroxylated fused quartz from contact angle measurements using some particular organics as probe liquids. Journal of Optoelectronics and Advanced Materials 2013;15(7–8) 627–634.

[166] Della Volpe C., Siboni S. In: Mittal K.L. (ed.). Acid–Base Interactions: Relevance to Adhesion Science and Technology. Utrecht: VSP BV; 2000. p55–p90.

[167] Pashley R.M., Kitchener J.A.J. Surface forces in adsorbed multilayers of water on quartz. Colloid Interface Science 1979;71(3) 491–500.

[168] Lamb R.N., Furlong D.N. Controlled wettability of quartz surfaces. Journal of the Chemical Society, Faraday Transactions 1982;78(1) 61–73.

[169] Beica T., Moldovan R., Zgura I., Frunza S., Poterasu M. Mechanism of homeotropic alignment of a doped liquid crystal. Journal of Optoelectronics and Advanced Materials 2006;8(4) 1512–1515.

[170] Kuo H.-F., Lien D.-H., Hsu W.K. Nondipolar liquid migration on carbon nanotube films at low field. Applied Physics Letters 2006;89(4) 044109.

[171] Carré A. Polar interactions at liquid/polymer interfaces. Journal of Adhesion Science and Technology. 2007;21(10) 961–981.

[172] Roy R.K., Lee K.R. Biomedical applications of diamond-like carbon coatings: a review. Journal of Biomedical Materials Research Part B: Applied Biomaterials. 2007;83(1) 72–84.

[173] Ostrikov K., Cvelbar U., Murphy A.B. Plasma nanoscience: setting directions, tackling grand challenges. Journal of Physics D: Applied Physics. 2011;44(17) 174001.

[174] Fedel M., Motta A., Maniglio D., Migliaresi C. Surface properties and blood compatibility of commercially available diamond-like carbon coatings for cardiovascular devices. Journal of Biomedical Materials Research Part B: Applied Biomaterials. 2009;90B(1) 338–349.

[175] Kocourek T., Jelınek M., Vorlıcek V., Zemek J., Janca T., Zızkova V., Podlaha J., Popov C. DLC coating of textile blood vessels using PLD. Applied Physics A. 2008;93(3) 627–632.

[176] Kwok S.C.H., Wang J., Chu P.K. Surface energy, wettability, and blood compatibility phosphorus doped diamond-like carbon films. Diamond and Related Materials. 2005;14(1) 78–85.

[177] Ma W.J., Ruys A.J., Mason R.S., Martin P.H., Bendavid A., Liu Z.W., Ionescu M., Zreiqat H. DLC coatings: effects of physical and chemical properties on biological response. Biomaterials. 2007;28(9) 1620–1628.

[178] Jones M.I., McColl I.R., Grant D.M., Parker K.G., Parker T.L. Protein adsorption and platelet attachment and activation on TiN, TiC and DLC coatings on titanium for cardiovascular applications. Journal of Biomedical Materials Research. 2000;52(2) 413–421.

[179] Okpalugo T.I.T., Ogwu A.A., Maguire P.D., McLaughlin J.A.D. Platelet adhesion on silicon modified hydrogenated amorphous carbon films. Biomaterials. 2004;25(2) 239–245.

[180] Yan X.B., Xu T., Yang S.R., Liu H.W., Xue Q.J. Characterization of hydrogenated diamond-like carbon films electrochemically deposited on a silicon substrate. Journal of Physics D: Applied Physics. 2004;37(17) 2416–2424.

[181] Okpalugo T.I.T., Papakonstantinou P., Murphy H., McLaughlin J., Brown N.M.D. High resolution XPS characterization of chemical functionalized MWCNTs and SWCNTs. Carbon. 2005;43(1) 153–161.

[182] Liao J.X., Liu W.M., Xu T., Xue Q.J. Characteristics of carbon films prepared by plasma-based ion implantation. Carbon. 2004;42(2) 387–393.

[183] Bugaev S.P., Korotaev A.D., Oskomov K.V., Sochugov N.S. Properties of diamond-like films obtained in a barrier discharge at atmospheric pressure. Technical Physics. 1997;42(8) 945–949.

[184] Riccardi C., Barni R., Fontanesi M., Tosi P. Gaseous precursors of diamond-like carbon films in CH4/Ar plasmas. Chemical Physics Letters. 2000;329(1–2) 66–70.

[185] Valentini L., Kenny J.M., Mariotto G., Tosi P. Deposition of hydrogenated amorphous carbon films from CH4/Ar plasmas: Ar dilution effects. Journal of Materials Science. 2001;36(21) 5295–5300.

[186] Owens D.K., Wendt R.C. Estimation of the surface free energy of polymers. Journal of Applied Polymer Science. 1969;13(8) 1741–1747.

[187] Roy R.K., Choi H.W., Yi J.W., Moon M.W., Lee K.R., Han D.K., Shin J.H., Kamijo A., Hasebe T. Hemocompatibility of surface-modified, silicon-incorporated, diamond-like carbon films. Acta Biomaterialia. 2009;5(1) 249–256.

[188] Liu Y., Li Z., He Z., Chen D., Pan S. Structure and blood compatibility of tetrahedral amorphous hydrogenated carbon formed by a magnetic-field-filter plasma stream. Surface and Coatings Technology. 2007;201(15) 6851–6856.